

Quantification of bedform dynamics and bedload sediment flux in sandy braided rivers from airborne and satellite imagery

| | |
|-------------------------------|---|
| Journal: | <i>Earth Surface Processes and Landforms</i> |
| Manuscript ID | ESP-18-0183.R2 |
| Wiley - Manuscript type: | Special Issue Paper |
| Date Submitted by the Author: | n/a |
| Complete List of Authors: | Strick, Robert; University of Brighton, School of Env and Technology Ashworth, Philip; University of Brighton, School of Env and Technology Sambrook Smith, Greg; university of Birmingham, Geography, Earth and Environmental Sciences Nicholas, Andrew; Exeter University, Geography; Best, Jim; University of Illinois, Departments of Geology and Geography and Ven Te Chow Hydrosystems Laboratory Lane, Stuart; Université de Lausanne, Institute of Earth Surface Dynamics Parsons, Daniel; University of Hull, Geography Simpson, Chris; University of Brighton, School of Environment and Technology Unsworth, Chris; University of Exeter College of Life and Environmental Sciences, Geography Dale, Jonathan; University of Brighton, School of Environment and Technology |
| Keywords: | sandy braided rivers, UAV, digital surface model, bedforms, bedload transport |
| | |

SCHOLARONE™
Manuscripts

1
2
3 **1 Quantification of bedform dynamics and bedload sediment flux in**
4
5
6 **2 sandy braided rivers from airborne and satellite imagery**
7
8

9 **3 Robert J.P. Strick¹, Philip J. Ashworth¹, Gregory H. Sambrook Smith², Andrew**
10
11 **4 P. Nicholas³, James L. Best⁴, Stuart N. Lane⁵, Daniel R. Parsons⁶, Christopher**
12
13 **5 J. Simpson¹, Christopher A. Unsworth³, Jonathan Dale¹**
14
15
16
17
18

19 ¹Division of Geography and Geology, School of Environment and Technology,
20
21 University of Brighton, Brighton, BN2 4GJ, UK
22

23
24 ²School of Geography, Earth, Environmental Sciences, University of Birmingham,
25
26 Edgbaston, Birmingham, BL5 2TT, UK
27

28
29 ³Geography, College of Life and Environmental Science, University of Exeter, Exeter
30
31 EX4 4RJ, UK
32

33
34 ⁴Departments of Geology, Geography and Geographic Information Science,
35
36 Mechanical Science and Engineering and Ven Te Chow Hydrosystems Laboratory,
37
38 University of Illinois at Urbana-Champaign, 1301 W. Green St., Urbana, IL 61801,
39
40 USA
41
42
43

44
45 ⁵Institute of Earth Surface Dynamics, Faculté des Géosciences et de
46
47 l'Environnement, Université de Lausanne, Bâtiment Géopolis, CH1015 Lausanne,
48
49 Switzerland
50

51
52 ⁶Department of Geography, Environment and Earth Science, Faculty of Science,
53
54 University of Hull, Hull, HU6 7RX, UK
55
56
57

58
59
60

23 ABSTRACT:

24 Images from specially-commissioned aeroplane sorties (manned aerial vehicle,
25 MAV), repeat unmanned aerial vehicles (UAVs) surveys, and Planet CubeSat
26 satellites are used to quantify dune and bar dynamics in the sandy braided South
27 Saskatchewan River, Canada. Structure-from-Motion (SfM) techniques and
28 application of a depth-brightness model are used to produce a series of Digital
29 Surface Models (DSMs) at low and near-bankfull flows. A number of technical and
30 image processing challenges are described that arise from the application of SfM in
31 dry and submerged environments. A model for best practice is outlined and analysis
32 suggests a depth-brightness model approach can represent the different scales of
33 bedforms present in sandy braided rivers with low-turbidity and shallow (< 2 m deep)
34 water.

35 The aerial imagery is used to quantify the spatial distribution of unit bar and
36 dune migration rate in an 18 km reach and three ~1 km long reaches respectively.
37 Dune and unit bar migration rates are highly variable in response to local variations
38 in planform morphology. Sediment transport rates for dunes and unit bars, obtained
39 by integrating migration rates (from UAV) with the volume of sediment moved (from
40 DSMs using MAV imagery) show near-equivalence in sediment flux. Hence, reach-
41 based sediment transport rate estimates can be derived from unit bar data alone.
42 Moreover, it is shown that reasonable estimates of sediment transport rate can be
43 made using just unit bar migration rates as measured from 2D imagery, including
44 from satellite images, so long as informed assumptions are made regarding average
45 bar shape and height. With recent availability of frequent, repeat satellite imagery,
46 and the ease of undertaking repeat MAV and UAV surveys, for the first time, it may
47 be possible to provide global estimates of bedload sediment flux for large or

1
2
3 48 inaccessible low-turbidity rivers that currently have sparse information on bedload
4
5 49 sediment transport rates.
6
7
8
9 50

10
11 51 KEYWORDS: Sandy braided rivers; UAV; drone; CubeSat; digital surface model;
12
13 52 bedforms; bedload transport; South Saskatchewan
14
15

16 17 53 **Introduction**

18
19
20 54 Over the past decade, considerable improvements in the quality, spatial scale,
21
22 55 frequency of capture, and resolution of remote sensing imagery, have enabled new
23
24 56 opportunities for investigating river morphodynamics (e.g., Lane *et al.*, 2010; Javernick
25
26 57 *et al.*, 2014; Ishiguro *et al.*, 2016; Vázquez-Tarrío *et al.*, 2017). In particular, the use
27
28 58 of unmanned aerial vehicles (UAVs) and Structure-from-Motion (SfM)
29
30 59 photogrammetry has become increasingly popular (Carrivick *et al.*, 2016; Kelleher *et*
31
32 60 *al.*, 2018). These techniques have been facilitated by advances in computer vision
33
34 61 software (Fonstad *et al.*, 2013), alongside the availability and low-cost of UAV
35
36 62 systems. However, significant variations in data quality, both between and within
37
38 63 surveys (Smith and Vericat, 2015) have been reported, stimulating a pressing need
39
40 64 for more rigorous and confidence-bounded data analysis methodologies (James *et al.*,
41
42 65 2017).
43
44
45
46
47

48 66 The use of UAVs and aerial images has improved our ability to quantify the
49
50 67 spatial organisation of river relief and bed roughness (e.g., Williams *et al.*, 2014;
51
52 68 Dietrich, 2016; James *et al.*, 2017; Carbonneau *et al.*, 2018), to track morphological
53
54 69 change over short time periods (Lane *et al.*, 1996, 2010; Palmsten *et al.*, 2015) and to
55
56 70 infer sediment transport rates (Lane *et al.*, 1995; Brasington *et al.*, 2003; Vericat *et al.*,
57
58 71 2017). However, a number of outstanding challenges remain. One of the main issues
59
60

1
2
3 72 with surveying rivers using photogrammetry is that unless the river is ephemeral, it is
4
5 73 a two-media environment (Lane *et al.*, 2000, 2010). Generating accurate elevations
6
7 74 for inundated river beds has proved problematic using SfM photogrammetric software
8
9 75 (Javernick *et al.*, 2014; Woodget *et al.*, 2015), a difficulty exacerbated in sandy river
10
11 76 environments where well-sorted silts and sands may give poor image texture (Lane *et*
12
13 77 *al.*, 2010).

14
15
16
17 78 However, if these technological and analytical challenges can be overcome,
18
19 79 these methods offer great potential for quantifying river process-form relationships.
20
21 80 For example, the field measurement of bedload flux (defined here as bed material in
22
23 81 continuous or intermittent contact with the bed) is notoriously difficult due to the
24
25 82 logistical difficulties of collecting data at high stage and the inherent spatial variability
26
27 83 in transport rates (Turowski *et al.*, 2010; Frings and Vollmer, 2017). This represents a
28
29 84 significant issue in terms of limiting the availability of data required to understand key
30
31 85 links between flow, morphology and sediment transport rates, which are essential for
32
33 86 parameterising and validating numerical models. To date, many estimates of bedload
34
35 87 sediment transport are thus restricted to relatively small and shallow rivers where point
36
37 88 samplers (i.e. Helley-Smith type samplers) or fixed location pit-type bedload traps
38
39 89 have been used. In addition, more spatially extensive estimates of sediment fluxes
40
41 90 have been generated using before and after flood topographic and lidar surveys (e.g.,
42
43 91 Goff and Ashmore, 1994; Brasington *et al.*, 2003; Anderson and Pitlick, 2014).
44
45 92 However, such repeat surveys may miss the record of successive erosion and
46
47 93 deposition events and largely lack detail on how sediment transport varies through a
48
49 94 flood (cf., Fuller *et al.*, 2003), or how it might link to the short-term evolution of bed and
50
51 95 barforms. The most detailed work on sediment flux has thus necessarily been limited
52
53 96 to physical experiments where detailed topographic surveys of the entire bed are
54
55
56
57
58
59
60

1
2
3 97 possible at high temporal and spatial resolution. While such experiments have
4
5 98 demonstrated that sediment flux in braided rivers may correlate with the migration rate
6
7 99 of bars within the channel (e.g., Wickert *et al.*, 2013) or the cyclic erosion and filling of
8
9 100 pools (e.g., Dhont and Ancey, 2018), this observation remains to be properly validated
10
11 101 in the field. The new technologies described above now provide an opportunity to
12
13 102 quantify the spatial distributions of bar and bedform migration rates in the field and
14
15 103 thus advance knowledge of how flow, morphology and sediment transport are linked.
16
17
18
19

20 104 This paper comprises two sections. The first details a number of
21
22 105 methodological procedures for analysing imagery in a sandy braided river
23
24 106 environment, whilst the second part illustrates how the resultant data can be used to
25
26 107 monitor and to interpret sand-bed river dynamics over short time periods (hours to
27
28 108 days). The objectives of this paper are thus to: (i) describe the processing steps and
29
30 109 challenges associated with using aerial imagery and SfM photogrammetry to produce
31
32 110 digital surface models (DSMs) in a sandy braided river with complex submergent and
33
34 111 emergent relief; (ii) develop and refine a depth-brightness model to allow quantification
35
36 112 of submerged elevations; (iii) use the resulting data to quantify the spatial variability of
37
38 113 dune and bar migration rates; and (iv) assess the potential for using repeat aerial and
39
40 114 satellite imagery of bed morphological change to map bedform and reach-scale
41
42 115 sediment transport rates in a sand-bed braided river.
43
44
45
46
47
48
49
50

116

117 **Study site**

51
52
53
54 118 The field-site detailed herein is the South Saskatchewan River, Canada, which is the
55
56 119 location where the 'classic' facies model for sandy, braided rivers was developed as
57
58 120 first proposed by Cant (1978) and Cant and Walker (1976, 1978). The river has a
59
60

1
2
3 121 range of scales of different sand bedforms (Sambrook Smith *et al.*, 2006; Best *et al.*,
4
5 122 2006; Lunt *et al.*, 2013), active bedload transport through most anabranches at a range
6
7 123 of flow stages, and has been the subject of previous analysis both of planform change
8
9 124 (e.g. Lane *et al.*, 2010; Parker *et al.*, 2013) but also sediment preservation and channel
10
11 125 belt sedimentology (e.g., Woodward *et al.*, 2003; Ashworth *et al.*, 2011; Lunt *et al.*,
12
13 126 2013). The low suspended sediment concentrations within the water column provide
14
15 127 optimal conditions for assessing the potential for using aerial imagery to quantify
16
17 128 bedform dynamics and morphological change.
18
19
20
21

22 129 The South Saskatchewan River flows from the Rocky Mountains in Alberta,
23
24 130 Canada, into Lake Diefenbaker, 25 km upstream of the study site at Outlook,
25
26 131 Saskatchewan (Figure 1A-B). Figure 1C shows the extent of the study site reported in
27
28 132 this paper, which is divided into two main sections, upstream and downstream of the
29
30 133 town of Outlook. Three smaller study reaches are reported in this paper termed 'SS1',
31
32 134 'SS2' and 'SS3' (see labels in Figure 1C). The Gardiner Dam traps much of the very
33
34 135 fine sediment so that the downstream river flow is clear and therefore the river bed is
35
36 136 entirely visible at even moderate flows. Previous work has shown that bed degradation
37
38 137 downstream of the Gardiner Dam is minimal at the site of the study reaches (Helfrick,
39
40 138 1993; Phillips, 2003). The study reaches are ~600 m wide, have an average bed slope
41
42 139 of 0.0003 and possess a very well sorted medium sand bed ($D_{50} = 0.3$ mm) with
43
44 140 negligible clay. The channels are dominated by ripples and dunes with lobate unit bars,
45
46 141 typically ~1.5 m in height (Sambrook Smith *et al.*, 2006).
47
48
49
50
51
52
53
54
55

56 143 **Data sources**

57
58
59
60

1
2
3 144 Three types of airborne imagery were used to quantify and to monitor morphological
4
5 145 change in the South Saskatchewan River: (i) specially-commissioned airplane sorties
6
7 146 (manned aerial vehicle, termed here 'MAV') over an 18 km-long stretch of the river; (ii)
8
9 147 UAV surveys over defined sub-reaches up to 1 km long; and (iii) satellite data from the
10
11 148 Planet CubeSat constellation (Planet Team, 2017; <https://www.planet.com>). The
12
13 149 following sections describe the process of image acquisition and data processing.
14
15

16 17 18 150 **Aerial (MAV) photography to generate whole reach DSMs**

19
20
21 151 Conventional aerial plane images (~0.06 m ground resolution) were captured at a
22
23 152 height of ~1500 m from a fixed-wing aeroplane with an UltraCamXp sensor for 2015,
24
25 153 2016 and two dates in 2017 (Table 1). The flight lines for the 2015 images were single
26
27 154 straight corridor flights down the river valley (similar to Lane *et al.*, 2010), whereas
28
29 155 those in 2016 and 2017 possessed 'back and forth' flight lines, which resulted in
30
31 156 greater image overlap (see Table 1). The greater overlap allows for better image
32
33 157 matching in the initial processing of the SfM program Pix4D (<https://pix4d.com/>) that
34
35 158 was employed throughout the analysis reported here.
36
37
38
39

40 159 Images are supplied with GPS information from the aircraft, along with Omega,
41
42 160 Phi, and Kappa (rotations in the XYZ-axis respectively) to aid in the initial processing.
43
44 161 In theory, ground control points (GCPs) are not necessary with such information, but
45
46 162 analyses suggest that the SfM process tends to produce tilt and/or doming unless
47
48 163 additional effort is made to constrain the SfM solution even with high grade
49
50 164 photogrammetric cameras (Bakker and Lane, 2017). A series of GCPs (crosses on 1
51
52 165 x 1 m targets with the centre of each cross occupying between 1 and 2 pixels) were
53
54 166 therefore laid out on the floodplain and bar surfaces immediately prior to the overhead
55
56 167 flight (Figure 2). GCP locations were measured with a Leica 1230 real-time kinematic
57
58
59
60

1
2
3 168 differential GPS, precise to ± 0.02 m horizontally and ± 0.03 m vertically. Fewer GCPs
4
5
6 169 were surveyed in 2017 because the water level was much higher, resulting in less
7
8 170 exposed bar surfaces on which to place targets.
9

11 171 **Verifying bedform morphology from water depth measurements**

12
13
14 172 Water depth and bed height were quantified in 2015, 2016 and 2017, using a
15
16 173 NAVISOUND 215 single beam echosonar (SBES) unit with a 200 kHz transducer
17
18 174 deployed from a small rib boat. The SBES operates at a vertical resolution of 0.01 m
19
20
21 175 and a ping rate of 5 Hz, with the SBES surveys being located using the Leica 1230
22
23 176 dGPS system. The echosonar had a blanking distance of 0.15 m and was typically set
24
25 177 0.1 m below the water surface resulting in the minimum water depth that could be
26
27
28 178 recorded as 0.25 m. SBES data were corrected for any dGPS errors associated with
29
30 179 lost radio links and spikes in the depth data series, using a range of <0.3 m and >4 m.
31
32 180 The SBES transects were conducted concurrent to the aerial sorties as well as at other
33
34 181 times, across a variety of locations and depths in order to capture a range of different
35
36 182 dune and bar morphologies present in the river.
37
38
39

40 183 **Fixed-wing UAV image collection to quantify bedform dynamics**

41
42
43 184 Two fixed-wing unmanned aerial vehicles (UAVs) were used to collect repeat aerial
44
45 185 imagery to quantify short-term bed evolution. Initial surveys in 2016 used the [eBee](#)
46
47 186 [RTK](#) but this was replaced in 2017 by the [eBee Plus](#). Flight lines were completed on
48
49 187 a grid pattern. Trials demonstrated that an 80% lateral and longitudinal overlap of
50
51 188 images was optimal for creating orthomosaics. Such large overlap values were
52
53 189 required due to the extensive areas of water within the study reach (Javernick *et al.*,
54
55 190 2014; Dietrich, 2016).
56
57
58
59
60

1
2
3 191 Multiple flights were flown at 90 m altitude and one-hour intervals (maximum
4
5 192 of five epochs in a day) to allow tracking of bedforms that could move at over 1 m hr⁻¹
6
7 193 (Table 2). The overall quality of the images collected was affected by the presence of
8
9 194 large areas of open water within the image capture zone and weather conditions at
10
11 194 large areas of open water within the image capture zone and weather conditions at
12
13 195 the time of flight. Excessive wind will both impact the ability of the UAV to stay on
14
15 196 course (both eBee RTK and eBee Plus can operate in wind speeds up to 10 m s⁻¹)
16
17 197 and will also generate water surface waves that reduce visibility through the water
18
19 198 column. The time of day and overall ambient light levels also affect the quality of the
20
21 199 images due to surface shimmer and illumination. Table 2 summarises the UAV sorties
22
23 200 used in this paper and the quality and number of epochs collected during the 2016
24
25 201 and 2017 field seasons. Ground Sampling Distance (GSD) was typically 0.025 - 0.03
26
27 202 m (Table 2) depending on the flight parameters and subsequent processing steps.
28
29 203 Figure 3 shows the spatial extent of the various UAV sorties in the 'downstream' reach
30
31 204 (Figure 1C).
32
33
34
35

36 205 **CubeSat Images**

37
38
39 206 In order to compare the results obtained from the MAV and UAV tracking of barforms
40
41 207 with independent satellite data, we conducted preliminary analysis of high-resolution
42
43 208 (~3.5 m) 4-band imagery available from the Planet CubeSat constellation (Planet
44
45 209 Team, 2017). This data source provides frequent (weekly to daily) imaging of much of
46
47 210 the Earth's surface, and allows the tracking of features that show change over such
48
49 211 timescales. Three epochs of satellite imagery were obtained from Planet for the period
50
51 212 of the MAV and UAV surveys and where cloud cover was minimal – on June 7th, June
52
53 213 12th and June 28th. The images for the entire survey area were imported into Global
54
55 214 Mapper where rectification was checked and adjusted where required using identical
56
57 215 features within the image area. The position of unit bar fronts for the 18 km study reach
58
59
60

1
2
3 216 was traced manually for each epoch. This yielded a sequence of 125 unit bars whose
4
5 217 migration could be traced, and allowed the method of bar migration applied to the MAV
6
7
8 218 and UAV imagery (see below) to also be applied to these CubeSat images.
9

10 219 **Water level measurement**

11
12
13 220 Water level in the study reaches was measured at one-minute intervals using multiple
14
15 221 Solinst© pressure transducers (precise to ± 3 mm) mounted on dexion frames within
16
17 222 the downstream reach and geolocated with dGPS. Corrections were made for
18
19 223 atmospheric pressure via a Solinst© barometer. Figure 4 shows the water level
20
21 224 variation during the period of data collection in the study reaches in June 2017. Daily
22
23 225 water releases from the upstream Gardiner Dam for power generation during peak
24
25 226 demand resulted in a diurnal water level fluctuation with maximum fluctuations of ~ 0.2
26
27 227 m typically in the early morning hours each day.
28
29
30
31
32

33 228

34 35 36 229 **Point Cloud and DSM generation and orthomosaic production from** 37 38 39 230 **aerial imagery**

40
41
42 231 Images collected from the MAV sorties were used to produce DSMs (see Figure 5 for
43
44 232 workflow). The processing protocols are described below together with an overview of
45
46 233 the technical challenges and procedures adopted to overcome them.
47
48
49

50 234 **Point cloud generation**

51
52
53 235 Point clouds and orthomosaics were created in the Structure-from-Motion (SfM)
54
55 236 program Pix4D with the 'large frame' supplementary software package. In the first
56
57 237 stage of processing, key points (tie points in classical photogrammetry) were extracted
58
59 238 from across the images available. As the images already contained some geolocation

1
2
3 239 information, the ground control point data were not added initially. A first bundle
4
5 240 adjustment was undertaken using Pix4D's key point matching system optimised for
6
7
8 241 aerial nadir imagery. Camera properties were specified using calibration certificates
9
10 242 and were not allowed to vary during calculation. Once a solution had been obtained,
11
12 243 the GCPs were added, using the WGS84 / UTM zone 13N (egm96) coordinate system.
13
14 244 At this point, the precision of the bundle adjustments was compared with the
15
16 245 theoretical precision defined by the image scale, and as the two were found to be of
17
18 246 the same order of magnitude, the bundle adjustments were accepted. Then, the point
19
20 247 cloud was derived. Matching was set to be to a lower density than the image resolution
21
22 248 (25%) to avoid redundancy in determined elevations.
23
24
25

26 27 249 **Tilt correction**

28
29
30 250 Even with imagery acquired with a photogrammetric standard camera with precisely
31
32 251 known focal distance, principal point offsets and lens distortion, and a reliable bundle
33
34 252 adjustment, random error in the bundle adjustment can translate into systematic error,
35
36 253 or tilt, in the DSM surface (Lane *et al.*, 2004; Bakker and Lane, 2017). To check
37
38 254 whether the DSMs contained residual tilt, elevation error values were derived by
39
40 255 comparing the dGPS elevation values from the GCPs with the DSM elevation
41
42 256 estimates at the GCP locations. Figures 6A-B show the relationship between elevation
43
44 257 error and Northing (approximately equivalent to distance along the valley axis) for two
45
46 258 DSMs. Figure 6A shows a DSM that is free from systematic tilt error. Figure 6B shows
47
48 259 a DSM with a systematic tilt error of c. 0.04 m km^{-1} in the Northing direction (assuming
49
50 260 no significant tilt in the Eastward direction). To correct the DSM for the occurrence of
51
52 261 systematic tilt, a manual and iterative approach is used to fit a 3D (X, Y, Z) modelled
53
54 262 error plane (represented by red dots in Figures 6A-B) to the elevation error values
55
56 263 (blue dots in Figures 6A-B). For the case where the DSM contains no systematic tilt,
57
58
59
60

1
2
3 264 for example a fitted trend surface with no Northing dependence (Figure 6A), then no
4
5 265 correction is necessary. For the case where the DSM contains tilt such as a Northing
6
7 266 dependence (Figure 6B), the associated trend surface is used to correct the DSM. The
8
9 267 example in Figures 6A-B shows only the case of a potential Northing dependency, but
10
11 268 it should be noted that the error surface is a 3D plane that could also be titled along
12
13 269 the Easting.
14
15

16 17 270 **Low image texture**

18
19
20 271 Bakker and Lane (2017) demonstrate that image texture is a critical control on the
21
22 272 quality of SfM photogrammetry. Low image texture occurs when there is a
23
24 273 homogenous distribution of pixel values with poorly identifiable distinct pixel regions.
25
26 274 Low image texture can be a significant problem in sandy braided rivers where large
27
28 275 areas may comprise water and low-relief sand bars (Lane *et al.*, 2010). Some filtering
29
30 276 of erroneous points is thus required to create a more reliable reconstruction of the
31
32 277 mean elevation.
33
34
35

36
37 278 Points were filtered in MATLAB (point density was first reduced to 0.5 m) by
38
39 279 applying a Chauvenet-type criterion (Lane *et al.*, 2004). Individual elevation (z) values
40
41 280 were treated as noise and removed if;
42
43
44

45 281 *Equation 1*

$$46
47 282 \quad z - \bar{z} > m\sigma_z$$

48
49
50 283 where \bar{z} and σ_z are the mean and standard deviation of the point elevation values
51
52 284 within a 35 pixel filtering window (17.5 m with the 0.5 m resampled grid) and m is equal
53
54 285 to 2. Elevation points that were removed were replaced by the mean elevation value
55
56 286 in a 3 x 3 pixel window centred on the point that was removed. The filtered point cloud
57
58 287 was interpolated via kriging in ArcGIS to produce the initial DSM. The DSM was then
59
60

1
2
3 288 classified into wet and dry areas so the former could be corrected for the refraction of
4
5 289 water. A water surface was created by interpolating points from along bar and bank
6
7 290 edges in the DSM. This water surface was used to identify (1) data points that are
8
9 291 submerged and so need refraction correction; and (2) the water depth of those points.
10
11 292 The refraction caused by water was then corrected by multiplying the newly created
12
13 293 depths for each pixel by a refraction index of 1.34 (Westaway *et al.*, 2000, 2001).
14
15 294 These new depths were then subtracted from the water surface to create the corrected
16
17 295 river bed elevations. The wet bed elevations were then merged with the dry DSM to
18
19 296 create the overall initial DSM for the reach.
20
21
22
23
24
25 297
26
27

28 298 **Depth-Brightness model in aerial (MAV) imagery**

29
30
31 299 The above method relies upon the principle that it is possible to obtain a dense number
32
33 300 of correct matches in inundated zones. As already shown for this kind of environment,
34
35 301 this may be a challenge (Figure 7, see also Lane *et al.*, 2010) even though the images
36
37 302 themselves show a rich level of morphological detail (e.g. Figure 1D). For this reason,
38
39 303 a second approach to depth determination was also employed, based upon depth-
40
41 304 brightness relationships, that is used quite widely for deriving stream bed bathymetry
42
43 305 from aerial imagery (e.g., Gilvear *et al.*, 1995; Winterbottom and Gilvear, 1997;
44
45 306 Westaway *et al.*, 2003; Legleiter *et al.*, 2004; Carbonneau *et al.*, 2006; Marcus and
46
47 307 Fonstad, 2008; Legleiter, 2016).
48
49
50
51

52 308 **Application**

53
54
55 309 A depth-brightness model predicts flow depth based on image pixel brightness (based
56
57 310 on the absorption of light as it passes through the water; Gilvear *et al.*, 1995). If light
58
59
60

1
2
3 311 with an incoming intensity I_{in} passes through a water depth of x , the remaining outgoing
4
5 312 intensity I_{out} can be estimated as:

6
7
8 313 *Equation 2*

9
10
11 314
$$I_{out} = I_{in} e^{-cx}$$

12
13
14 315 where c is the rate of light absorption by water, which varies with turbidity and
15
16 316 frequency of the incident light (Carbonneau *et al.*, 2006). Using calibration data from
17
18 317 SBES and manual depth measurements, which were taken as close as possible to the
19
20 318 time of image acquisition, the relationship between water depth and pixel log
21
22 319 brightness was modelled using linear regression. Changes in water level between the
23
24 320 times of image capture and the depth measurement surveys were accounted for by
25
26 321 applying a linear depth correction, based on data from the water level recorders.

27
28
29
30
31 322 Depth values were plotted in a GIS superimposed on a log brightness image,
32
33 323 so that depth measurement locations could be matched precisely to the corresponding
34
35 324 pixel value. Once the pixel values had been extracted, log brightness values were
36
37 325 plotted against the corresponding depth values to create the depth-brightness
38
39 326 relationship (Figure 8). The linear equation from this relationship was then used to
40
41 327 convert the log brightness values from the orthomosaic into water depths.

42
43
44
45 328 The depth-brightness derived depths were subtracted from the water surface
46
47 329 (created earlier) to produce river bed elevations, which were then merged with the
48
49 330 DSM. This creates a combined DSM of SfM emergent elevations and depth-brightness
50
51 331 submerged bed elevations.

52
53
54
55 332 **Pixel colour saturation**

1
2
3 333 One of the limitations of using a depth-brightness model is that for depths > 2 m colour
4
5 334 saturation occurs in the image and depths can no longer be estimated accurately
6
7 335 (Lane *et al.*, 2010). Analysis of the extensive SBES data set from 2016 (747,756 points
8
9 336 distributed over 18 km) shows that only 7.5% of values surveyed for the South
10
11 337 Saskatchewan River were greater than 2 m depth (Figure 9). However, these SBES
12
13 338 data are biased towards deeper areas because of boat access and the need for rapid
14
15 339 surveys of active dune fields. A better comparison is probably the proportion of
16
17 340 saturated pixels in the total wetted area of the DSMs which is 1% in 2016 and 1.5%
18
19 341 for 2017. This confirms that although this method of DSM production may not be
20
21 342 suitable for deeper rivers, it works well to represent the majority of river bed elevations
22
23 343 for the South Saskatchewan River.
24
25
26
27
28

29 344 **Water surface reflection**

30
31
32 345 An additional factor that can affect the quality of the depth-brightness model is surface
33
34 346 reflection (Overstreet and Legleiter, 2017) that produces speckles of white on aerial
35
36 347 imagery (see the white dots in Figure 10). These specks are converted into large
37
38 348 spikes in the depth-brightness model and subsequently derived DSMs. Problems can
39
40 349 exist due to DSM-related mismatches that then cause incorrect local orthoimage
41
42 350 production, typically associated with areas of expansive water. This can leave poorly
43
44 351 reconstructed areas in the orthomosaic, or even gaps (Figure 10), caused by Pix4D
45
46 352 having difficulties in identifying matching points in inundated zones. The constant
47
48 353 movement of the water surface also causes slight differences in the pixel values, as
49
50 354 well as minor changes in illumination.
51
52
53
54
55

56 355 Removal of these artefacts from the bed elevations produced by the depth-
57
58 356 brightness model was achieved by converting the bed elevation raster DSM into
59
60

1
2
3 357 points. These points were then subjected to universal kriging with a constant order of
4
5 358 trend removal, exponential Kernel, and a lag size of 1 with 31 lags. These parameters
6
7 359 maintained the bed morphology, removed the large spikes caused by surface
8
9 360 reflection and also filled any holes in the orthomosaics.

361 **Accounting for pixel discolouration**

362 An additional challenge with using a depth-brightness model occurs where the spectral
363 properties of the bed vary significantly, leading to a breakdown of the assumption that
364 the optical signature of a point is only a function of water depth. For example, where
365 there is a change in sediment type from sand to gravel, or there is a build-up of biofilm,
366 there will be a change in spectral properties. This can result in darker pixels
367 (associated with biofilms, for example) at similar depths to lighter pixels (associated
368 with sand). The consequence of this is that the brightness model predicts greater
369 depths for these darker areas than is the case in reality. To help overcome this
370 problem, a difference map was generated between the depths from the DSM created
371 using Pix4D and those from the depth-brightness model and any zones with a
372 consistent difference of more than 1 m were masked. This resulted in 12% of masking
373 in the 2016 wetted area portions of the DSM. Generally, these zones were in shallow
374 water, which is where the original Pix4D DSM performed best (Figure 7). Therefore,
375 the Pix4D DSM was laid on top of the brightness model in these zones. This issue was
376 particularly prevalent in the 2016 images when biofilm growth was extensive following
377 a warm spring period.

378 **Shadow effects**

379 Depending on the time of image acquisition, there is a possibility that shadows behind
380 topography (e.g. dune crests, bar fronts, boulders) can cause pixel discolouration

1
2
3 381 (darkening) that then translates into a perceived 'over deepening' of the bed. There
4
5 382 was thus a trade-off between flying early or late in the day (low sun angle but more
6
7 383 shadows) versus near midday (high sun angle but more surface glare). All aeroplane
8
9 384 (MAV) images (that were used for DSM construction) were acquired around 10.00 and
10
11 385 15.00 with a low sun angle. Comparison of echosonar surveys taken immediately after
12
13 386 the MAV image acquisition with DSMs from the MAV aerial orthomosaics shows the
14
15 387 shadowing, and thus potential overdeepening, is a maximum of 30% (worse-case
16
17 388 scenario) and averages 10-20%, but it only impacts 1-2 pixels adjacent to the crest of
18
19 389 topographic highs.
20
21
22
23
24
25
26
27

28 391 **Error analysis and validation for the plane imagery**

30 392 **DSM error analysis**

31
32
33
34 393 The following error analysis is for the DSMs created from the MAV imagery. It
35
36 394 compares the z values from field dGPS surveys from exposed/emergent topography,
37
38 395 on or 24 hours after the aerial photography flight, to the z values for the same location
39
40 396 as estimated from the DSMs (n = 13-76 for the different reaches and epochs, see
41
42 397 Table 4). Although the root mean square error (RMSE) is reported for comparison to
43
44 398 other studies, the standard deviation of error (SDE) is used for the main error analysis
45
46 399 as RMSE conflates systematic (mean) and random (standard deviation) errors, which
47
48 400 are different parameters. Table 4 shows that the SDE ranged from ± 0.08 m to ± 0.19
49
50 401 m for the different DSMs and SDE/GSD ranged from ± 1.33 m to ± 3.17 m, which is
51
52 402 very similar to the range of values reported for other studies (see Table 5).
53
54
55
56
57

58 403 **Depth-brightness model evaluation**

59
60

1
2
3 404 The performance of the depth-brightness model was evaluated by comparison with
4
5 405 equivalent SBES and dGPS data. Comparing the average dune heights measured
6
7 406 from the SBES data to those measured from the DSM, showed no significant
8
9 407 difference (Paired T-Test, $p = 0.078$) between the two different methods, giving
10
11 408 confidence in the ability of the brightness model to recreate accurately the bedform
12
13 409 height. Additionally, dGPS measured depth points were compared to those estimated
14
15 410 from the brightness-model DSM in the downstream reach for June 8th 2017 (Figure
16
17 411 11). The SDE for the brightness DSM points was ± 0.17 m, which is similar to the
18
19 412 overall DSM SDE value of ± 0.12 m (Table 4).
20
21
22
23
24

25 413 **DOD error analysis**

26
27
28 414 When comparing two different DSMs, it is critical to understand the survey
29
30 415 uncertainties and potential error propagation between the two surfaces (James *et al.*,
31
32 416 2017). Additionally, when using DSMs of difference (DoDs), changes smaller than a
33
34 417 specified 'level of detection' (LoD) should be omitted from analysis. The LoD can be
35
36 418 defined using (Lane *et al.*, 2003):
37
38
39

40 419 *Equation 3*

$$42 43 44 45 46 47 48 49 50 51 52 53 54 55 56 57 58 59 60$$
$$LoD = \pm t(\sigma_{z1}^2 + \sigma_{z2}^2)^{1/2}$$

46 421 where, σ_{z1} and σ_{z2} are the vertical standard deviations of error of the two DSMs used
47
48 422 to generate the DoD, and t is an appropriate value for the required confidence level,
49
50 423 typically 95% (1.96). A single LoD value (Table 4) can then be estimated from SDE.
51
52 424 However, depending on the distribution of points used in the SDE, significant smaller
53
54 425 changes that are spatially coherent over large areas may be neglected (Brasington *et*
55
56 426 *al.*, 2003). The errors reported for the different DSMs used in the present paper (see
57
58
59
60

427 SDE/GSD, Table 4) compare favourably to other studies (Table 5), bearing in mind
428 the different image scales.

429

430 **Measurement of unit bar and dune migration and estimates of** 431 **sediment transport rates from MAV and UAV imagery**

432 **Unit bar sediment transport rates from MAV imagery**

433 The orthomosaics created from the MAV images were used to trace the migration of
434 all unit bar avalanche faces for the entire reach between June 8th and June 12th 2017
435 (n = 295). Each visible unit bar avalanche face was digitised manually to produce a
436 bar front length (L) for each flight date. A polygon was then created by joining the bar
437 front positions from each date together and a planform area (A_b) of migration was
438 calculated. The migration rate for each bar between epochs t₁ and t₂ (M_b in m hr⁻¹)
439 was then calculated by:

440 *Equation 4*

$$441 M_b = A_b / \bar{L} (t_2 - t_1)$$

442 This methodology was also applied to the CubeSat satellite imagery.

443 In addition to quantifying unit bar migration rates, the average unit bar
444 migration direction was computed as the bearing (from north) of the centroids of each
445 bar crest as positioned in the images from 8th and 12th June 2017.

446 For the MAV imagery sediment transport rates of individual unit bars were
447 calculated with reference to the DoD produced for 8-12th of June 2017. The DoD
448 provided a volume of difference (V) between the two surfaces contained within each

1
2
3 449 polygon area. Sediment transport rate per unit width (Q_{sb} , $m^2 \text{ hr}^{-1}$) was calculated from
4
5 450 unit bar migration as:

6
7
8 451 *Equation 5*

$$9 \quad 452 \quad Q_{sb} = V (1-P)/L(t_2-t_1)$$

10
11
12
13
14 453 where P is the sediment porosity and is taken as 0.4 for well sorted sands (van Rijn
15
16 454 1993).

19 455 **Dune migration rates and estimated sediment transport rates from UAV imagery**

20
21
22 456 Dune migration rates were quantified from repeat UAV flights in reaches SS1 and SS2
23
24 457 (2016) and SS3 (2017) (see Figures 3A-B). Dune migration was quantified for
25
26 458 'patches' in each reach that varied in size from 340-5198 m^2 (see Table 6). Patch
27
28 459 locations were selected to provide a spatially-distributed dataset that represented the
29
30 460 different morphological elements and a range of local flow depths. Individual dune
31
32 461 migration rates were calculated using the dune crestlines identified in each
33
34 462 georectified orthomosaic and the same calculation procedure described above for unit
35
36 463 bars. Dune sediment transport rates per unit width (Q_{sd} , $m^2 \text{ hr}^{-1}$) were calculated for
37
38 464 individual dunes in each of the 20 patches of the SS3 2017 reach only (Figure 3B,
39
40 465 Table 6) as:

41
42
43
44
45 466 *Equation 6*

$$46 467 \quad Q_{sd} = (1-P) b H M_d$$

47
48
49 468
50
51
52 469 where

53
54
55 470 b is dune shape factor calculated as $A_d/(H \times \lambda)$

1
2
3 471 A_d is dune area calculated between the two successive troughs
4
5

6 472 H is dune height (from trough to crest)
7
8

9 473 λ is dune wavelength (from trough to trough)
10
11

12 474 M_d is dune migration rate calculated as for unit bars
13
14

15 475
16
17

18 476 Values of H and b were obtained for each dune from downstream profiles taken
19
20 477 through individual dunes using the brightness model DSM from the MAV images taken
21
22 478 on 12 June 2017. Dunes identified in the UAV images could be tied to the same dunes
23
24 479 in the MAV orthophoto/DSM because the MAV sortie was flown only 2 hours earlier.
25
26 480 Typically, the morphology of between 9 and 20 dunes was measured in each patch
27
28 481 depending on patch size and dune prevalence.
29
30
31

32 482
33
34

35 483 **Using aerial imagery to understand the dynamics of sand-bed**

36 484 **braided rivers**

37 485 **Sand-bed braided river morphology and change**

38
39
40
41
42 486 Despite the challenges of using airborne imagery to visualise and quantify river bed
43
44 487 topography, Figure 12 shows that the resulting DSMs are capable of representing well
45
46 488 the complex and multiple scales of bed topography that characterise sandy braided
47
48 489 rivers (e.g., Cant, 1978; Skelly *et al.*, 2003; Sambrook Smith *et al.*, 2006; Horn *et al.*,
49
50 490 2012). For example, the DSM (Figure 12) displays many small (label A), medium (label
51
52 491 B) and large (label C) 2D and 3D dunes, incipient unit bars (label D), exposed unit
53
54 492 bars with elongated bar tails (label E), and early-stage bar top hollows (labels F). With
55
56
57
58
59
60

1
2
3 493 a GSD of 0.06 m for the aerial imagery it is impossible to resolve bedforms at the scale
4
5 494 of ripples but it is possible to observe small superimposed dunes (label G). Even
6
7 495 though Figure 12 is just one snapshot in time, the resolution and therefore clarity of
8
9 496 the DSM, provides a valuable insight into the interrelationship between different
10
11 497 bedforms including the spatial transformation from 2D to 3D dunes and the
12
13 498 progressive response of dune planform shape and wavelength to a change in water
14
15 499 depth and unit bar emergence. The DSM (Figure 12) also illustrates that the South
16
17 500 Saskatchewan River can have some reaches that contain few dominant main
18
19 501 channels (although see discussion below). Except for the 20-40 m-wide channel on
20
21 502 the right of the reach (Figure 12, near label B), where there is ongoing bank erosion,
22
23 503 the DSM is characterised by a series of migrating and stacked unit bars.
24
25
26
27
28

29 504 Figure 13A shows the morphology of the South Saskatchewan River at a
30
31 505 different scale to that shown in Figure 12. Unlike Figure 12, the ~6 km-long reach at
32
33 506 low flow shows a dominant main channel that is mostly pinned against the west (left)
34
35 507 bank. The dominant thalweg splits and re-joins both around exposed unit bars and
36
37 508 major compound bars. The DoD over a period of 15 months (Figure 13B) shows
38
39 509 examples of bar head erosion (labelled H), lateral bar accretion of up to 2 m (labelled
40
41 510 M), thalweg scour up to 4 m (labelled T), and anabranch abandonment and filling
42
43 511 (labelled F) (cf., Lane *et al.*, 2010; Parker *et al.*, 2013). The majority of the compound
44
45 512 bars, and particularly those that are attached to the right bank (east), have not
46
47 513 aggraded appreciably and have been simply eroded at their upstream ends, with
48
49 514 deposition at their tail as the bars migrate slowly downstream (cf., Bristow, 1987;
50
51 515 Ashworth *et al.*, 2000; Best *et al.*, 2003; Nicholas, 2013; Schuurman and Kleinmans,
52
53 516 2015).
54
55
56
57
58
59
60

1
2
3 517 The average distribution of bed heights from the DSMs for the upstream
4
5 518 reach (Figure 13A) for the three years of aerial imagery (2015-2017) shows negligible
6
7 519 change (Figure 14) with an overall near-normal distribution and annual bed height
8
9 520 fluctuations between lower (2015) and higher (2017) average bed elevations. The
10
11 521 annual reach channel change (Figure 13B) can be contrasted with the DoD for the
12
13 522 four-day period in June 2017 when discharge was relatively high for the year (Figure
14
15 523 13C and 13D). There is little topographic change within this short time period
16
17 524 (represented by white colour shading in Figure 13D), but the DoD does clearly pick
18
19 525 out the migration of over 20 lobate, unit bar avalanche faces. Patches of local erosion
20
21 526 (Figure 13D: in yellow) are associated largely with thalweg migration and minor
22
23 527 channel adjustment although some of the bankside aggradation may be related to the
24
25 528 different illumination conditions for each flight that have caused pixel discolouration
26
27 529 (see discussion earlier). Taken together, Figures 13B 13D and Figure 14 suggest the
28
29 530 aerial imagery and processing is capturing and resolving both the short and longer-
30
31 531 term morphological changes in the dynamic South Saskatchewan River.

32 33 34 35 36 37 38 532 **Spatial variability in dune and unit bar migration rates**

39
40
41 533 Based on the UAV imagery from three study reaches (Fig. 15, Table 6) dune migration
42
43 534 rates range over an order of magnitude from 0.1 m hr⁻¹ to 1.0 m hr⁻¹. These rates are
44
45 535 towards the lower end of rates reported in previous work, for example 0.8 m hr⁻¹ for
46
47 536 the Fraser River, Canada (Villard and Church, 2005), 0.8-1.6 m hr⁻¹ for the Calamus
48
49 537 River, USA (Gabel, 1993), 1-2.7 m hr⁻¹ in the Gels A, Denmark (Kisling-Moller, 1992),
50
51 538 but up to ~100 m hr⁻¹ for highly mobile gravel dunes in the Toutle River, USA (Dinehart,
52
53 539 1989). The primary reach-scale morphological control on dune migration rate appears
54
55 540 to be the extent to which flow is either largely contained within a single channel or
56
57 541 more widely spread across the braidplain. This is most clearly illustrated by

1
2
3 542 comparison between reaches SS2 and SS3 (Figures 15B-C). For reach SS2, flow was
4
5 543 largely constrained within a single ~150 m-wide channel. In particular, the downstream
6
7 544 section of this channel was uniform in width and cross-sectional morphology
8
9
10 545 (encompassing the last four measurement patches) resulting in very similar dune
11
12 546 migration rates that only varied between 0.43 m hr⁻¹ and 0.53 m hr⁻¹. In contrast, reach
13
14 547 SS3 was constrained within one channel at its most upstream point before changing
15
16 548 to a braidplain > 500 m wide with multiple unit and compound bars. As the flow is
17
18 549 distributed across a much wider area, dune migration rates diminished from 1.15 m hr
19
20
21 550 ¹ at the head of the reach to a minimum of 0.13 m hr⁻¹ downstream of a sheltered bar
22
23 551 tail. Dune fields that approach actively accreting bar heads were also zones of high
24
25 552 dune migration rates as illustrated by reaches SS1 (Figure 15A) and SS3 (Figure 15C).

26
27
28
29 553 There was a difference in reach flow discharge when the dune migration
30
31 554 data were measured for the reaches shown in Figures 15A-C. For reaches SS1 and
32
33 555 SS2, the flow discharge through the reach was ~65m³s⁻¹, whereas for reach SS3 it
34
35 556 was ~275m³s⁻¹. Despite this four-fold difference in local discharge, the range in dune
36
37 557 migration rate was broadly similar for all reaches, suggesting that: (a) increases in
38
39 558 discharge simply spread water further across the braidplain, rather than further
40
41 559 concentrating flow in the deeper thalwegs, which might increase dune migration rates;
42
43 560 and (b) the main driver of the spatial changes in dune migration rates is the local
44
45 561 topography and multiple scales of roughness. Dune size has a finite range of variation
46
47 562 in these limited water depths that are similar between reaches, and that do not change
48
49 563 appreciably once the flow has reached bar-top level. Consequently, this limits the
50
51 564 range of dune sizes, and thus migration velocities, that are broadly similar between
52
53 565 reaches.
54
55
56
57
58
59
60

1
2
3 566 The migration rates for unit bars ($n = 295$) are typically an order of
4
5 567 magnitude lower than those of dunes, with an overall average of 0.06 m hr^{-1} . However,
6
7
8 568 as with the dune migration rates discussed above, variability exists between the
9
10 569 different bars studied, with a maximum of 0.32 m hr^{-1} . The spatial pattern of migration
11
12 570 rates, and therefore sediment transport rates for a given bar height, throughout the
13
14
15 571 river is characterised by high variability (Figure 16), although some trends are
16
17 572 apparent. The lowest migration rates are either largely found on the braidplain margins
18
19 573 away from the main channels or in compound bar tail areas, similar to the dunes
20
21
22 574 discussed above. The migration rates of unit bars also vary within different channels
23
24 575 that flow around a compound bar, presumably in response to flow steering around the
25
26 576 bar. For example, a central vegetated compound bar in Figure 16B has greater rates
27
28 577 of unit bar migration down the east (right) as compared with the west (left) channel.
29
30
31 578 Likewise, unit bar migration rates are often lower within cross-bar channels as
32
33 579 compared with the main thalwegs (e.g., lower part of Figure 16C).

34
35
36 580 The migration direction of unit bars is also highly variable (Figure 16D). Unit
37
38 581 bars typically migrate in directions ± 90 degrees to the 'downstream' direction of the
39
40 582 valley (shown as a shaded zone on Figure 16D) and the main channels. There is some
41
42
43 583 indication (Figure 16D) that these migration rates diminish when the unit bar
44
45 584 orientation deviates more than 30 degrees from the overall downstream direction,
46
47 585 perhaps reflecting the lower competence of cross-braidplain channels. These
48
49
50 586 quantitative measurements highlight the spatial complexity of sediment transport
51
52 587 within sandy braided rivers, and suggest that local factors such as changing flow
53
54 588 depths and flow steering, are likely critical in determining the spatial distribution of
55
56
57 589 sediment transport rates.

58
59
60 590 **Bedload sediment transport rates calculated from dune and unit bar migration**

1
2
3 591 For reach SS3, 20 patches (Figure 3B), comprising a total of 255 dunes were
4
5 592 monitored to calculate local bedload sediment transport rates using the morphological
6
7 593 measurements of each individual dune (see Equation 6). Average bed sediment
8
9 594 transport rate per unit width based on migration of these dunes was $0.016 \text{ m}^2 \text{ hr}^{-1}$, with
10
11 595 rates varying between $0.001 \text{ m}^2 \text{ hr}^{-1}$ and $0.134 \text{ m}^2 \text{ hr}^{-1}$. Within the same reach, and
12
13 596 over approximately the same time period, 19 unit bars were also used to estimate the
14
15 597 bed sediment transport rate (see Equation 5), yielding an average of $0.024 \text{ m}^2 \text{ hr}^{-1}$,
16
17 598 with rates varying between $<0.001 \text{ m}^2 \text{ hr}^{-1}$ and $0.100 \text{ m}^2 \text{ hr}^{-1}$. These dune and unit bar
18
19 599 derived rates are thus very similar and demonstrate that both methods return a bed
20
21 600 sediment transport rate per unit width of $\sim 0.02 \text{ m}^2 \text{ hr}^{-1}$. In addition, the unit bar bedload
22
23 601 transport rates were also calculated over the entire study reach, totalling 295 bars,
24
25 602 yielding a value of $0.02 \text{ m}^2 \text{ hr}^{-1}$, which is identical to that for the 19 unit bars used in
26
27 603 the analysis of reach SS3. However, a key difference between the dune and unit bar
28
29 604 bedload transport rates is in their distributions (Figure 17) that are positively skewed
30
31 605 but bimodal for dune and unit bar bedload transport rates respectively. Unit bar
32
33 606 bedload transport rates have $\sim 29\%$ of values $<0.0025 \text{ m}^2 \text{ hr}^{-1}$ and $\sim 17\%$ of values
34
35 607 $>0.05 \text{ m}^2 \text{ hr}^{-1}$.

36
37
38
39
40
41
42
43 608 There is also significant variability in bedload transport rates within reach
44
45 609 SS3, with a tendency for transport rates (calculated from dune migration) to be lower
46
47 610 downstream of unit bar fronts as compared with rates calculated from dunes migrating
48
49 611 on the stoss slope of unit bars. This attribute is most clearly illustrated by comparing
50
51 612 patches 5, 17, 18 and 8 (see labels in Figure 15C) that are on the stoss side of a
52
53 613 classic lobate fronted unit bar, and patch 10 (Figure 15C) that is downstream of the
54
55 614 unit bar front. The stoss side patch of dunes yields an average bed sediment transport
56
57 615 rate of $0.015 \text{ m}^2 \text{ hr}^{-1}$, while the leeside value is only $0.007 \text{ m}^2 \text{ hr}^{-1}$. Likewise patch 9
58
59
60

1
2
3 616 (Figure 15C), also downstream of a lobate fronted unit bar, and patch 14 (Figure 15C)
4
5 617 downstream of an assemblage of unit bars in an overall compound bar tail setting,
6
7 618 possess similarly low transport rates of 0.008 and $0.003 \text{ m}^2 \text{ hr}^{-1}$ respectively.
8
9

10
11 619

12 13 14 620 **The potential of using aerial imagery to quantify the dynamics of** 15 16 621 **sand-bed braided rivers** 17 18

19
20 622 Previous studies that have used UAV imagery coupled with SfM have highlighted the
21
22 623 potential problems in generating DSMs from inundated parts of the channel and
23
24 624 highlighted water depth, turbidity and turbulence as key limiting factors. For example,
25
26 625 Woodget *et al.* (2017) studied a small 3-13 m wide meandering gravel bed river, and
27
28 626 suggested a limit of 1.4 m depth for the methodology. Based on the addition of using
29
30 627 a depth-brightness model coupled with SfM, for low-turbidity waters, we suggest
31
32 628 herein that this upper limit can be extended to 2 m depth and for conventional MAV
33
34 629 imagery as well as UAV drone imagery. It should be noted that application of SfM,
35
36 630 together with a depth-brightness model, works well in the South Saskatchewan River
37
38 631 where suspended sediment loads are low due to the trapping of fine sediment by the
39
40 632 upstream Gardiner Dam. Bedform tracking in much deeper channels and higher
41
42 633 turbidity (e.g. in many of the world's largest rivers), may be more challenging unless
43
44 634 there are future significant technological advances (e.g. UAVs tethered to
45
46 635 miniaturised, boat-mounted, echo-sounders as illustrated by Alvarez *et al.* (2018);
47
48 636 Bandini *et al.* (2018)).
49
50
51
52
53

54
55 637 One advantage of using UAVs that has been demonstrated herein is that
56
57 638 because they are relatively simple and inexpensive to deploy, they provide an
58
59 639 excellent tool for elucidating the temporal morphodynamics of rivers. To date, most
60

1
2
3 640 studies have highlighted the improvement in spatial resolution that UAV imagery
4
5 641 provides, such as for habitat mapping (Woodget *et al.*, 2017) or detection of grain size
6
7 642 variation (e.g. Carbonneau *et al.*, 2018). The results described herein for a sand-bed
8
9 643 river, where sediment is being transported at most flow stages, demonstrates
10
11 644 unambiguously that in optimal conditions, bedform dynamics can be quantified at
12
13 645 hourly timescales and at both low and near-bankfull stages.
14
15
16
17

18 646 While the concept of dune tracking to estimate bedload transport rates has
19
20 647 a long history, this has traditionally been achieved using repeat bed profiles derived
21
22 648 from boat-based echosounder surveys (e.g. van den Berg, 1987; Ten Brinke *et al.*,
23
24 649 1999; Dinehart, 2002; Gaueman and Jacobson, 2007; Claude *et al.*, 2012) or at-a-
25
26 650 point with fixed depth profilers (Dinehart, 1989). The results described herein
27
28 651 demonstrate that in shallow, low-turbidity rivers, this approach also lends itself to
29
30 652 image analysis methods without the need for boat-based surveys and the logistical
31
32 653 challenges that involves. The ease with which drones can be deployed also means
33
34 654 that even in environments where dunes migrate rapidly, such as the South
35
36 655 Saskatchewan River, repeat surveys can be undertaken with sufficient frequency to
37
38 656 ensure dunes can be identified and tracked from one aerial survey epoch to the next,
39
40 657 before they lose their morphological coherence and visually recognisable form.
41
42
43
44
45

46 658 Although bedform tracking using repeat airborne imagery can yield
47
48 659 insightful quantification of the bedload sediment transport rate it should be noted these
49
50 660 estimates represent a minimum value. This is because not all sediment in transport
51
52 661 contributes to the migration of the dune or unit bar and some sediment is likely steered
53
54 662 around the bedform or temporarily passes into suspension over the lee face (see
55
56 663 discussion for the case of dunes in Mohrig and Smith (1996)). However, in bedload
57
58 664 dominated streams, such as gravel-bed rivers and the South Saskatchewan River, this
59
60

1
2
3 665 underestimation of bedload sediment transport rate (particles in continuous or
4
5 666 intermittent contact with the bed) is probably minimal.
6
7

8 667 The similarity between the mean bedload transport rates derived from both
9
10 668 dune and unit bar migration suggests that most of the sediment being transported by
11
12 669 unit bars is being supplied by dune migration over the stoss sides of the unit bars. A
13
14 670 similar conclusion was reached by Villard and Church (2005) in their study of bar and
15
16 671 dune dynamics in the Fraser River, Canada. This suggests that consideration of just
17
18 672 unit bar migration rates may enable estimation of bedload flux at the scale of the
19
20 673 channel width. In this case, a key consideration is the minimum area of study required
21
22 674 to generate a robust sediment transport estimate. Reach SS3 in the present study,
23
24 675 which was 685 m x 1190 m and contained 19 unit bars with measurable migration
25
26 676 rates, provides an indication of the likely minimum area required. For example, the
27
28 677 bedload sediment transport rate derived from the 19 unit bars in reach SS3 was the
29
30 678 same as for the 295 bars of the entire study area. This suggests that the measurement
31
32 679 reach was sufficiently large to capture the range of transport rates found throughout
33
34 680 the 18 km study area. As a guide, a reach length of ~ 3 x the braidplain width may be
35
36 681 a good approximation for the monitoring area required for a first-order estimate of
37
38 682 bedload sediment transport rate in such rivers. Whether this rule of thumb of optimal
39
40 683 reach size is transferable to other rivers requires further testing and may depend on
41
42 684 the local complexity of braidplain topography and prevalence of unit bars.
43
44
45
46
47
48
49

50 685 A final question is whether high-resolution DSMs and DoDs are actually
51
52 686 required to generate a robust average bedload sediment transport rate for a reach in
53
54 687 a river like the sandy braided South Saskatchewan. Generating simple rectified
55
56 688 orthomosaics from drone imagery is much quicker than generating DSMs, especially
57
58 689 for the submerged regions. In essence, can the sediment transport rate be generated
59
60

1
2
3 690 from just 2D imagery using the unit bar migration rate? To explore this question,
4
5 691 migration rates for the 19 unit bars of SS3 reach were all assigned the same shape
6
7 692 factor (0.5, although it is recognised that bars may have slightly higher values
8
9 693 depending on their aggradational history and migration rate), the same porosity (0.4
10
11 694 for sands) and given a bar height value of 1.25 m (an average value reported for the
12
13 695 South Saskatchewan River by Lunt *et al.*, (2013)). These bar attributes together with
14
15 696 the measured migration rate then allowed calculation of the bedload sediment
16
17 697 transport rate. The results reveal the average for the measurement reach was exactly
18
19 698 the same as that for where the shape and height of each unit bar was individually
20
21 699 established based on the DSMs. While this observation clearly needs additional
22
23 700 testing to assess its utility, it could revolutionise our ability to estimate reach-based
24
25 701 bedload sediment transport rates.
26
27
28
29
30

31 702 To provide a preliminary test of this idea, we used three epochs for June
32
33 703 7th, 12th and 28th 2017 from the 3.5 m resolution satellite imagery of the South
34
35 704 Saskatchewan River provided by the CubeSat constellation of Planet.com
36
37 705 (PlanetTeam, 2017). This imagery (Figure 18) clearly shows the position of unit bars
38
39 706 within the river and allows their crestlines to be tracked between epochs (see colour
40
41 707 lines on Figures 18A, B and C), although dunes cannot be discerned. The migration
42
43 708 rates obtained from these images (Figure 18D) over a 21-day time period show a
44
45 709 comparable range of values to the UAV and MAV imagery, with mean migration rates
46
47 710 of 0.062 and 0.088 m hr⁻¹ for the UAV/MAV and Planet images respectively (both with
48
49 711 standard deviations of 0.055 m hr⁻¹). The distribution of migration rates is more skewed
50
51 712 to smaller values for the UAV/MAV estimates (Figure 18D), probably due to the
52
53 713 difficulty of delineating smaller unit bars in the coarser-resolution satellite imagery.
54
55 714 Although dunes in the South Saskatchewan River cannot be resolved in these
56
57
58
59
60

1
2
3 715 CubeSat images, such bedforms may be resolved in larger rivers (so long as turbidity
4
5 716 levels are low), where dune size may range up to many metres in height and tens to
6
7 717 hundreds of metres in wavelength (e.g., see Galeazzi *et al.*, 2018 for details of such
8
9 718 dunes in the Amazon River). In this case, dune migration rates may also be
10
11 719 quantifiable, although the results herein suggest that estimation of solely the unit bar
12
13 720 migration rates may yield comparable results.
14
15
16
17

18 721 In addition, the pixel resolution of the satellite imagery also dictates the
19
20 722 period between epochs that will allow slower migrating bars to be quantified. To
21
22 723 demonstrate this contention, the distribution of migration rates for short (5 days) and
23
24 724 long (21 days) temporal gaps between Planet images (Figure 18E inset) shows that,
25
26 725 at this spatial resolution (3.5 m), slower migration rates can only be quantified at longer
27
28 726 temporal spacings. The shorter temporal period of five days is unable to capture
29
30 727 migration rates of less than $\sim 0.06 \text{ m hr}^{-1}$ (see grey shaded area in Figure 18E).
31
32
33

34 728 The utility of using such frequent satellite imagery thus relies on: i) cloud-
35
36 729 free skies; ii) the spatial resolution of the sensor with respect to both the epoch
37
38 730 frequency and bar migration rates, and iii) detection of unit bar fronts in flows that may
39
40 731 be deep and turbid. However, if these conditions can be addressed satisfactorily, or
41
42 732 technological advances can solve these challenges, such frequent satellite imagery
43
44 733 opens up the possibility of estimating bedload sediment transport rates for
45
46 734 inaccessible rivers, both large and small, where there is currently a dearth of data.
47
48 735 This may improve our ability to estimate bedload sediment flux in rivers across the
49
50 736 globe, and its spatial and temporal variation. Such a data requirement is central to
51
52 737 addressing issues of channel change, anthropogenic influences on sediment transport
53
54 738 and channel morphology, validating and improving numerical models of longer-term
55
56 739 channel change and helping guide river channel management (Best, 2018).
57
58
59
60

1
2
3 740
4
5
6 741 **Conclusions**
7
8
9
10 742 Four principal conclusions can be drawn from the work reported herein. First, airplane
11 743 (MAV) and drone (UAV) aerial imagery can be used with Structure-from-Motion (SfM)
12 744 processing techniques, and application of a depth-brightness model, to generate
13 745 robust DSMs for sandy braided rivers at flows near bankfull and with depths up to 2
14 746 m. The importance of following best practice in the application of SfM techniques is
15 747 pivotal here, including collecting ground control data, checking for residual tilt in the
16 748 analysis, and suitable filtering of acquired data. In addition, the present study confirms
17 749 the value of using the optical richness of underwater zones to produce extremely
18 750 detailed topographic data, and proposes a series of solutions to address the problems
19 751 that can arise in doing so (e.g. reflection at the water surface, spatial variability in
20 752 bottom reflection). Second, dune and bar migration rates and directions in sandy
21 753 braided rivers are highly variable spatially, with evidence for local planform
22 754 morphology determining some of this variability. Third, bedload sediment transport
23 755 estimated from unit bar migration rates broadly integrates the sediment supplied by
24 756 the dunes migrating over their stoss sides, such that reach-based estimates of bedload
25 757 sediment transport rates can be estimated from unit bar data alone. Fourth,
26 758 reasonable estimates of bedload sediment transport may be possible from just unit
27 759 bar migration as measured from 2D imagery, including from satellites, and
28 760 assumptions regarding average bar shape and height. With further technological
29 761 advances, such a methodology could revolutionise our ability to provide global
30 762 estimates of bedload sediment flux from large and/or inaccessible rivers that are
31 763 currently very poorly quantified.
32
33
34
35
36
37
38
39
40
41
42
43
44
45
46
47
48
49
50
51
52
53
54
55
56
57
58
59
60

1
2
3 764
4
5
6 765
7
8

9 766 *Acknowledgements* - PJA, APN, DAP and GSS thank the UK Natural Environment
10
11 767 Research Council (NERC) for grants NE/L00738X/1, NE/L005662/1, NE/L00450X/1,
12
13 768 NE/L005441/1 that funded this work. Vance and Janine Ylioja kindly gave us access
14
15 769 to their land and boat launch, whilst Bill Vavra generously provided storage facilities
16
17 770 and access to his land. Bob and Sandy Stephenson at the Irrigation Motel in Outlook
18
19 771 provided invaluable assistance and logistical support. Dwight Thies gave insightful
20
21 772 advice on the initial UAV surveys and helped with fieldwork. We thank Planet.com for
22
23 773 access to, and use of, CubeSat imagery, and particularly Joe Mascaro for his advice
24
25 774 and guidance on use of this imagery. Image processing was performed using
26
27 775 Pix4Dmapper software under an educational licence (Pix4D SA, Switzerland). We
28
29 776 thank Chris Fielding and an anonymous reviewer for their insightful comments and
30
31 777 suggestions.

32 778 **References**

- 33
34
35
36
37
38
39 779 Alvarez LV, Moreno HA, Segales AR, Pham TG, Pillar-Little EA, Chilson PB. 2018.
40
41 780 Merging Unmanned Aerial Systems (UAS) imagery and echo soundings with an
42
43 781 adaptive sampling technique for bathymetric surveys. *Remote Sensing* **10**. DOI:
44
45 782 10.3390/rs10091362
46
47
48
49 783 Anderson S, Pitlick J. 2014. Using lidar to estimate sediment transport in a steep
50
51 784 stream. *Journal of Geophysical Research Earth Surface* **119**(3): 621-643. DOI:
52
53 785 10.1002/2013JF002933.
54
55
56
57 786 Ashworth PJ, Sambrook Smith GH, Best JL, Bridge JS, Lane SN, Lunt IA, Reesink
58
59 787 AJH, Simpson CJ, Thomas RE. 2011. Evolution and sedimentology of a channel
60

- 1
2
3 788 fill in the sandy braided South Saskatchewan River and its comparison to the
4
5 789 deposits of an adjacent compound bar. *Sedimentology* **58**(7): 1860-1883.
6
7
8 790 DOI:10.1111/j.1365-3091.2011.01242.x.
9
10
11 791 Bakker M, Lane SN. 2017. Archival photogrammetric analysis of river-floodplain
12
13 792 systems using Structure from Motion (SfM) methods. *Earth Surface Processes*
14
15 793 *and Landforms* **42**: 1274-1286. DOI: [10.1002/esp.4085](https://doi.org/10.1002/esp.4085).
16
17
18 794 Bandini F, Olesen D, Jakobsen J, Kittel CMM, Wang, S, Garcia M, Bauer-Gottwein
19
20 795 P. 2018. Technical note: Bathymetry observations of inland water bodies using a
21
22 796 tethered single-beam sonar controlled by an unmanned aerial vehicle.
23
24
25 797 *Hydrological and Earth System Sciences* **22**: 4165-4181. DOI: 10.5194/hess-22-
26
27 798 4165-2018
28
29
30 799 Best JL. In press. Anthropogenic stresses on the World's big rivers. *Nature*
31
32 800 *GeoScience*
33
34
35 801 Best JL, Ashworth PJ, Bristow CS, Roden J. 2003. Three-dimensional sedimentary
36
37 802 architecture of a large, mid-channel sand braid bar, Jamuna River, Bangladesh.
38
39 803 *Journal of Sedimentary Research* **73**: 516–530.
40
41
42
43 804 Best J, Woodward J, Ashworth PJ, Sambrook Smith G, Simpson C. 2006. Bar top
44
45 805 hollows: A new element in the architecture of sandy braided rivers. *Sedimentary*
46
47 806 *Geology* **190**: 241-255. DOI: 10.1016/j.sedgeo.2006.05.022.
48
49
50
51 807 Brasington J, Langham J, Rumsby B. 2003. Methodological sensitivity of
52
53 808 morphometric estimates of coarse fluvial sediment transport. *Geomorphology*
54
55 809 **53**(3): 299-316. DOI: 10.1016/S0169-555X(02)00320-3.
56
57
58
59
60

- 1
2
3 810 Bristow CS. 1987. Brahmaputra River: channel migration and deposition. In: *Recent*
4
5 811 *Developments in Fluvial Sedimentology*, (Etridge, FG, Flores RM, Harvey MD,
6
7 812 eds.), Special Publication Society Economic Palaeontology and Mineralogy, **39**:
8
9 813 63–74.
10
11
12
13 814 Cant DJ, Walker RG. 1976. Development of a braided fluvial facies model for the
14
15 815 Devonian Battery Point Sandstone, Quebec, Canada. *Canadian Journal of Earth*
16
17 816 *Sciences* **13**: 102–119. DOI.org/10.1139/e76-010.
18
19
20 817 Cant DJ. 1978. Bedforms and bar types in the South Saskatchewan River. *Journal of*
21
22 818 *Sedimentary Petrology* **48**: 1321–1330. DOI: 10.1306/212F7676-2B24-11D7-
23
24 819 8648000102C1865D.
25
26
27
28 820 Cant DJ, Walker RG, 1978. Fluvial processes and facies sequences in the sandy
29
30 821 braided South Saskatchewan River, Canada. *Sedimentology* **25**: 625–648. DOI:
31
32 822 10.1111/j.1365-3091.1978.tb00323.x.
33
34
35 823 Carbonneau PE, Lane SN, Bergeron B. 2006. Feature based image processing
36
37 824 methods applied to bathymetric measurements from airborne remote sensing in
38
39 825 fluvial environments. *Earth Surface Processes and Landforms* **31**: 1413–1423.
40
41 826 DOI: 10.1002/esp.1341.
42
43
44
45 827 Carbonneau PE, Bizzi S, Marchetti G. 2018. Robotic photosieving from low-cost
46
47 828 multirotor sUAS: a proof-of-concept. *Earth Surface Processes and Landforms*
48
49 829 DOI:10.1002/esp.4298.
50
51
52
53 830 Carrivick J, Smith M, Quincey D. 2016. Structure from motion in the geosciences:
54
55 831 New Analytical Methods in Earth and Environmental Science. Wiley Blackwell,
56
57 832 208 pp.
58
59
60

- 1
2
3 833 Chauvenet W. 1960. *A Manual of Spherical and Practical Astronomy* V. II. 1863.
4
5 834 Reprint of 1891. 5th ed. Dover, N.Y.: 474-566.
6
7
8 835 Claude N, Rodrigues S, Bustillo V, Bréhéret J-G, Macaire J-J, Jugé P. 2012.
9
10 836 Estimating bedload transport in a large sand–gravel bed river from direct
11
12 837 sampling, dune tracking and empirical formulas. *Geomorphology* **179**: 40-57.
13
14
15
16 838 Dhont B, Ancey C. 2018. Are bedload transport pulses in gravel-bed rivers created
17
18 839 by bar migration or sediment waves? *Geophysical Research Letters* **45**:5501-
19
20 840 5508. Doi.org/10.1029/2018GL077792.
21
22
23 841 Dietrich JT. 2016. Riverscape mapping with helicopter-based structure-from-motion
24
25 842 photogrammetry. *Geomorphology* **252**:144-157.
26
27 843 Doi.org/10.1016/j.geomorph.2015.05.008.
28
29
30
31 844 Dinehart RL. 1989. Dune migration in a steep, coarse-bedded stream. *Water*
32
33 845 *Resources Research* **25** (5): 911-923.
34
35
36 846 Fonstad MA, Dietrich JT, Courville BC, Jensen JL, Carbonneau PE. 2013.
37
38 847 Topographic structure from motion: a new development in photogrammetric
39
40 848 measurement. *Earth Surface Processes and Landforms* **38**(4): 421–430.
41
42 849 DOI:10.1002/esp.3366.
43
44
45
46 850 Frings RM, Vollmer S. 2017. Guidelines for sampling bedload transport with
47
48 851 minimum uncertainty. *Sedimentology* **64**: 1630-1645. doi: 10.1111/sed.12366.
49
50
51 852 Fuller IC, Large ARG, Charlton ME, Heritage GL, Milan DJ. 2003. Reach-scale
52
53 853 sediment transfers: An evaluation of two morphological budgeting approaches.
54
55 854 *Earth Surface Processes and Landforms* **28**: 889-903.
56
57
58
59
60

- 1
2
3 855 Gabel SL. 1993. Geometry and kinematics of dunes during steady and unsteady
4
5 856 flows in the Calamus River, Nebraska, USA. *Sedimentology* **40**: 237-269.
6
7
8 857 Gaeuman D, Jacobson RB. 2007. Field assessment of alternative bed-load
9
10
11 858 transport estimators. *Journal of Hydraulic Engineering* **133**(12): DOI:
12
13 859 10.1061/(ASCE)0733-9429(2007)133:12(1319)
14
15
16 860 Galay VJ, Pentland RS, Halliday RA. 1985. Degradation of the South Saskatchewan
17
18 861 River below Gardiner Dam. *Canadian Journal of Civil Engineering* **12**: 849-862.
19
20
21
22 862 Galeazzi CP, Almeida RP, Mazoca CEM, Best JL, Freitas BT, Ianniruberto M,
23
24 863 Cisneros J, Tamura LN. 2018. The significance of superimposed dunes in the
25
26 864 Amazon River: Implications for how large rivers are identified in the rock record.
27
28 865 *Sedimentology*. Doi: 10.1111/sed.12471.
29
30
31
32 866 Gilvear DJ, Waters TM, Milner AM. 1995. Image-analysis of aerial-photography to
33
34 867 quantify changes in channel morphology and instream habitat following placer
35
36 868 mining in interior Alaska. *Freshwater Biology* **34**: 389-398.
37
38
39 869 Goff JR, Ashmore PE. 1994. Gravel transport and morphological change in the
40
41 870 braided Sunwapta River, Alberta, Canada. *Earth Surface Processes and*
42
43 871 *Landforms* **19**: 195-212.
44
45
46
47 872 Horn JD, Fielding CR, Joeckel RM. 2012. Revision of Platte River alluvial facies
48
49 873 model through observations of extant channels and barforms, and subsurface
50
51 874 alluvial valley fills *Journal of Sedimentary Research*. **82**: 72-91.
52
53
54 875 Ishiguro S, Yamano H, Oguma H. 2016. Evaluation of DSMs generated from multi-
55
56 876 temporal aerial photographs using emerging structure from motion-multi-view
57
58
59
60

- 1
2
3 877 stereo technology. *Geomorphology* **268**: 64-71.
4
5 878 DOI:10.1016/j.geomorph.2016.05.029.
6
7
8 879 James MR, Robson S, Smith MW. 2017. 3-D uncertainty-based topographic change
9
10 880 detection with structure-from-motion photogrammetry: precision maps for ground
11
12 881 control and directly georeferenced surveys. *Earth Surface Processes and*
13
14 882 *Landforms* **42**: 1769-1788. DOI: 10.1002/esp.4125
15
16
17
18 883 Javernick L, Brasington J, Caruso B. 2014. Modelling the topography of shallow
19
20 884 braided rivers using Structure-from-Motion photogrammetry. *Geomorphology*
21
22 885 **213**: 166–182. DOI:10.1016/j.geomorph.2014.01.006.
23
24
25
26 886 Kelleher C, Scholz CA, Condon L, Reardon M. 2018. Drones in geoscience
27
28 887 research: The sky is the only limit. *Eos* **99**, DOI: 10.1029/2018EO092269.
29
30
31 888 Kisling-Moller, K. 1992. Lateral sediment transport by bedforms in a meander bend.
32
33 889 *Earth Surface Processes and Landforms* **17**: 501-513.
34
35
36 890 Lane SN, Westaway RM, Hicks DM. 2003. Estimation of erosion and deposition
37
38 891 volumes in a large gravel-bed, braided river using synoptic remote sensing.
39
40 892 *Earth Surface Processes and Landforms* **28**, 249-71.
41
42
43
44 893 Lane SN, Reid SC, Westaway RM, Hicks DM. 2004. Remotely sensed topographic
45
46 894 data for river channel research: the identification, explanation and management
47
48 895 of error. In: Kelly REJ, Drake NA, Barr SL. *Spatial Modelling of the Terrestrial*
49
50 896 *Environment*, Wiley, Chichester, 157-174.
51
52
53
54 897 Lane SN, Richards KS, Chandler JH. 1995. Morphological estimation of the time-
55
56 898 integrated bedload transport rate. *Water Resources Research* **31**(3):761-772.
57
58 899 DOI: 10.1029/94WR01726.
59
60

- 1
2
3 900 Lane SN, Richards KS, Chandler JH. 1996. Discharge and sediment supply controls
4
5 901 on erosion and deposition in a dynamic alluvial channel. *Geomorphology* **15**: 1-
6
7 902 15. DOI: 10.1016/0169-555X(95)00113-J.
8
9
10 903 Lane SN, Widdison PE, Thomas RE, Ashworth PJ, Best JL, Lunt IA, Sambrook
11
12 904 Smith GH, Simpson CJ. 2010. Quantification of braided river channel change
13
14 905 using archival digital image analysis. *Earth Surface Processes and Landforms*
15
16 906 **35**(8): 971–985. DOI:10.1002/esp.2015.
17
18
19
20 907 Lane SN. 2000. The measurement of river channel morphology. *Photogrammetric*
21
22 908 *Record*. **16**: 937-961. DOI: 10.1111/0031-868X.00159.
23
24
25
26 909 Legleiter CJ, Roberts DA, Marcus WA, Fonstad MA. 2004. Passive optical remote
27
28 910 sensing of river channel morphology and in-stream habitat: physical basis and
29
30 911 feasibility. *Remote Sensing of Environment* **93**: 493-510.
31
32
33
34 912 Legleiter CJ. 2016. Inferring river bathymetry via Image-to-Depth Quantile
35
36 913 Transformation (IDQT). *Water Resources Research* **52**: 3722-3741. DOI:
37
38 914 10.1002/2016WR018730
39
40
41 915 Lunt IA, Sambrook Smith GH, Best JL, Ashworth PJ, Lane SN, Simpson CJ. 2013.
42
43 916 Deposits of the sandy braided South Saskatchewan River: Implications for the
44
45 917 use of modern analogs in reconstructing channel dimensions in reservoir
46
47 918 characterization. *American Association of Petroleum Geologists Bulletin* **97**(4):
48
49 919 553-576. DOI: 10.1306/09251211152.
50
51
52
53 920 Marcus WA, Fonstad MA. 2008. Optical remote mapping of rivers at sub-meter
54
55 921 resolutions and watershed extents. *Earth Surface Processes and Landforms* **33**:
56
57 922 4-24.
58
59
60

- 1
2
3 923 Mohrig D, Smith JD. 1996. Predicting the migration rates of subaqueous dunes.
4
5 924 *Water Resources Research* **32**(10): 3207-3217. DOI: 10.1029/96WR01129
6
7
8 925 Nicholas AP. 2013. Modelling the continuum of river channel patterns. *Earth Surface*
9
10 926 *Processes and Landforms* **38**: 1187-1196. DOI: 10.1002/esp.3431
11
12
13 927 Overstreet BT, Legleiter CJ. 2017. Removing sun glint from optical remote sensing
14
15 928 images of shallow rivers. *Earth Surface Processes and Landforms* **42**: 318-333
16
17
18 929 Palmsten ML, Kozarek JL, Calantoni J. 2015. Video observations of bed form
19
20 930 morphodynamics in a meander bend. *Water Resources Research* **51**: 7238-
21
22 931 7257. DOI: 10.1002/2014WR016321.
23
24
25 932 Parker NO, Sambrook Smith GH, Ashworth PJ, Best JL, Lane SN, Lunt LA, Simpson
26
27 933 CJ, Thomas RE. 2013. Quantification of the relationship between surface
28
29 934 morphodynamics and subsurface sedimentological product in sandy braided
30
31 935 rivers. *Sedimentology* **60**(3): 820-839. DOI: 10.1111/j.1365-3091.2012.01364.x.
32
33
34 936 Phillips RTJ. 2003. *Downstream geomorphic impacts of reservoir construction on the*
35
36 937 *sand-bed braided South Saskatchewan River, Saskatchewan*. Unpublished
37
38 938 B.Sc. (Hons) thesis, Simon Fraser University, BC, Canada, 75 pp.
39
40
41 939 Planet Team 2017. Planet Application Program Interface: In Space for Life on Earth.
42
43 940 San Francisco, CA. <https://api.planet.com>
44
45
46 941 Sambrook Smith GH, Ashworth PJ, Best JL, Woodward J, Simpson CJ. 2006. The
47
48 942 alluvial architecture and sedimentology of the sandy, braided South
49
50 943 Saskatchewan River, Canada *Sedimentology* **53**: 413-434. DOI: 10.1111/j.1365-
51
52 944 3091.2005.00769.x.
53
54
55
56
57
58
59
60

- 1
2
3 945 Schuurman F, Kleinhans MG. 2015. Bar dynamics and bifurcation evolution in a
4
5 946 modelled braided sand-bed river. *Earth Surface Processes and Landforms* **40**:
6
7 947 1318-1333. DOI: 10.1002/esp.3722.
8
9
10 948 Skelly RL, Bristow CS, Ethridge FG. 2003. Architecture of channel-belt deposits in
11
12 949 an aggrading shallow sandbed braided river: the lower Niobrara River, northeast
13
14 950 Nebraska. *Sedimentary Geology* **158**: 249–270.
15
16
17
18 951 Smith MW, Vericat D. 2015. From experimental plot to experimental landscapes:
19
20 952 topography, erosion and deposition in sub-humid Badlands from Structure-from-
21
22 953 Motion photogrammetry. *Earth Surface Processes and Landforms* **40**: 1656-
23
24 954 1671. DOI: 10.1002/esp.3747.
25
26
27
28 955 Smith MW, Carrivick JL, Hooke J, Kirkby MJ. 2014. Reconstructing flash flood
29
30 956 magnitudes using 'Structure-from-motion': A rapid assessment tool. *Journal of*
31
32 957 *Hydrology* **519**: 1914-1927. DOI: 10.1016/j.jhydrol.2014.09.078.
33
34
35
36 958 Ten Brinke, WBM, Wilbers AWE, Wesseling C. 1999. Dune growth, decay and
37
38 959 migration rates during a large-magnitude flood at a sand and mixed sand-gravel
39
40 960 bed in the Dutch Rhine river system, *Special Publication of the International*
41
42 961 *Association of Sedimentologists* **28**: 15-32.
43
44
45
46 962 Turowski JM, Rickenmann D, Dadson SJ. 2010. The partitioning of the total
47
48 963 sediment load of a river into suspended and bedload: a review of empirical data.
49
50 964 *Sedimentology* **57**: 1126-1146.
51
52
53 965 van Rijn LC. 1993. *Principles of Sediment Transport in Rivers, Estuaries and Coastal*
54
55 966 *Seas*, Aqua, Amsterdam.

- 1
2
3 967 van den Berg JH.1987. Bedform migration and bed-load transport in some rivers and
4
5 968 tidal environments. *Sedimentology* **34**: 681-698 DOI: 10.1111/j.1365-
6
7 969 3091.1987.tb00794.x
8
9
10 970 Vázquez-Tarrío D, Borginet L, Liébault F, Recking A. 2017. Using UAS optical
11
12 971 imagery and SfM photogrammetry to characterize the surface grain size of
13
14 972 gravel bars in a braided river (Vénéon River, French Alps). *Geomorphology* **285**:
15
16 973 94-105. DOI: 10.1016/j.geomorph.2017.01.039.
17
18
19 974 Vericat D, Wheaton JM, Brasington J. 2017. Revisiting the morphological approach:
20
21 975 opportunities and challenges with repeat high-resolution topography. *Gravel-Bed*
22
23 976 *Rivers: Process and Disasters* (Tsutsumi D, Laronne JB, eds). 121-158. DOI:
24
25 977 10.1002/9781118971437.ch5.
26
27
28 978 Villard PV, Church M. 2005. Bar and dune development during a freshet: Fraser
29
30 979 River Estuary, British Columbia, Canada. *Sedimentology* **52**: 737-756.
31
32
33 980 Westaway RM, Lane SN, Hicks, DM. 2000. The development of an automated
34
35 981 correction procedure for digital photogrammetry for the study of wide, shallow,
36
37 982 gravel-bed rivers. *Earth Surface Processes and Landforms* **25**: 209–226.
38
39
40 983 Westaway RM, Lane SN, Hicks, DM. 2001. Remote sensing of clear-water, shallow,
41
42 984 gravel-bed rivers using digital photogrammetry. *Photogrammetric Engineering &*
43
44 985 *Remote Sensing* **67**:1271-1281.
45
46
47 986 Westaway RM, Lane SN, Hicks DM. 2003. Remote survey of largescale braided,
48
49 987 gravel-bed rivers using digital photogrammetry and image analysis. *International*
50
51 988 *Journal of Remote Sensing* **24**(4): 795–815. DOI:10.1080/01431160110113070.
52
53
54
55
56
57
58
59
60

- 1
2
3 989 Wickert AD, Martin JM, Tal M, Kim W, Sheets W, Paola C. 2013. River channel
4
5 990 lateral mobility: metrics, time scales, and controls. *Journal of Geophysical*
6
7 991 *Research* **118**(2): 396-412. DOI: 10.1029/2012JF002386.
8
9
10 992 Williams RD, Brasington J, Vericat D, Hicks DM. 2014. Hyperscale terrain modelling
11
12 of braided rivers: fusing mobile terrestrial laser scanning and optical bathymetric
13 993 mapping. *Earth Surface Processes and Landforms* **39**: 167–183. DOI:
14 994 10.1002/esp.3437.
15
16
17 995
18
19
20 996 Winterbottom SJ, Gilvear DJ. 1997. Quantification of channel bed morphology in
21
22 gravel-bed rivers using airborne multispectral imagery and aerial photography.
23 997 *Regulated Rivers-Research & Management* **13**: 489-499.
24
25 998
26
27
28 999 Woodget AS, Austrums R, Maddock IP, Habit E. 2017. Drones and digital
29
30 1000 photogrammetry: from classifications to continuums for monitoring river habitat
31
32 and hydromorphology. *WIREs Water*, **4**: n/a, e1222. doi:10.1002/wat2.1222
33 1001
34
35
36 1002 Woodget AS, Carbonneau PE, Visser F, Maddock IP. 2015. Quantifying submerged
37
38 1003 fluvial topography using hyperspatial resolution UAS imagery and structure from
39
40 1004 motion photogrammetry. *Earth Surface Processes and Landforms* **40**: 47-64
41
42 1005 DOI: 10.1002/esp.3613
43
44
45 1006 Woodward J, Ashworth PJ, Best JL, Sambrook Smith GH, Simpson CJ. 2003. The
46
47 1007 use and application of GPR in sandy fluvial environments: methodological
48
49 1008 considerations. In: *Ground Penetrating Radar in Sediments* (Bristow CS, Jol HM,
50
51 1009 eds), **211**: 127-142.
52
53
54
55 1010
56
57
58
59
60

1
2
3 1011 **Figure captions**
4
5

6 1012 Figure 1: A) location within Canada, B) study site location within Saskatchewan
7
8 1013 Province, C) upstream and downstream reaches at study site including the three
9
10 1014 study reaches described in this paper: SS1, SS2 and SS3, and D) close up of
11
12 1015 upstream and downstream reaches (taken in 2016).
13
14

15
16 1016 Figure 2: Distribution of GCPs on 2015 upstream and 2017 upstream reaches.
17

18
19 1017 Figure 3: A) location of 2016 dune migration measurements in SS1 and SS2 reaches
20
21 1018 and B) 2017 dune migration measurements in SS3 reach. Dotted line shows the
22
23 1019 boundary of UAV coverage.
24
25

26 1020 Figure 4: Water level variations during the 2017 field season and at the times of
27
28 1021 airplane and UAV flights. Notice the daily variations in water level associated with the
29
30 1022 release of water from the Gardiner Dam.
31
32

33
34 1023 Figure 5: Workflow of DSM production from aerial images and the various data
35
36 1024 sources and computer programmes employed.
37
38

39 1025 Figure 6: Elevation error plotted against Northing value for DSMs that are free from
40
41 1026 systematic tilt error (A) and which contain systematic tilt error (B). Blue circles
42
43 1027 represent the elevation error (difference between DSM and GCP elevation values)
44
45 1028 prior to tilt correction. Red circles represent the modelled error plane that is used to
46
47 1029 correct the DSM for the presence of systematic tilt.
48
49

50
51 1030 Figure 7: SfM becomes unreliable in producing bed elevations when water depths
52
53 1031 are greater than 1.6 m, thus justifying the need for a depth-brightness model. Note
54
55 1032 the scale is the local (z) datum and the boundary of 1.6 m depth has been
56
57
58
59
60

1
2
3 1033 superimposed to show the inconsistency of submerged bed elevations when only
4
5 1034 SfM is employed.

6
7
8 1035 Figure 8: An example of a depth-brightness model used to create river bed depths
9
10 1036 from aerial (MAV) orthomosaics. This particular model is for the June 8th 2017 flight
11
12
13 1037 and was created using SBES depth measured points.

14
15
16 1038 Figure 9: Histogram of SBES depths collected during the 2016 field season, note
17
18 1039 that very few depths (7.5%) are greater than 2 m.

19
20
21 1040 Figure 10: Issue with the depth-brightness model showing specks from surface
22
23 1041 shimmer and holes from the orthomosaic.

24
25
26 1042 Figure 11: A) Example of points from depth measured error, and B) histogram for the
27
28 1043 June 8th DSM 2017.

29
30
31 1044 Figure 12: River bed depths superimposed on the orthomosaic showing detail of the
32
33 1045 various sand bedforms (see key). Location of image is in reach SS1 (see Figure 3A)

34
35
36
37 1046 Figure 13: A) orthomosaic of the upstream 2016 reach at low flow (discharge at time
38
39 1047 of image acquisition = $\sim 85 \text{ m}^3 \text{ s}^{-1}$); B) DSM of difference (DoD) of the 2016 upstream
40
41 1048 reach minus the 2015 upstream reach, green to blue is deposition, yellow to red is
42
43 1049 erosion (labels are described in the text); C) orthomosaic of the upstream 2017
44
45 1050 reach at high flow (discharge at time of image acquisition = $\sim 395 \text{ m}^3 \text{ s}^{-1}$); and D)
46
47 1051 DoD of June 12th 2017 minus June 8th 2017 DSMs.

48
49
50
51 1052 Figure 14: Elevation distributions for the 2015, 2016, and 2017 upstream reaches.

52
53
54 1053 Figure 15: Dune migration rates for reaches SS1 (A), SS2 (B) and SS3 (C). Labels
55
56 1054 within circles in Figure 15C refer to the measurement patches also described in
57
58 1055 Table 6.

1
2
3 1056 Figure 16: Bar unit sediment transport rates calculated from repeat airplane sorties in
4
5 1057 June 2017 for the upstream reach (A), the first half of the downstream reach (B), and
6
7 1058 the last half of the downstream reach (C). Unit bar migration rates and directions for
8
9
10 1059 all the bars shown in Figures 16A-C are shown in (D). Note the centre of the
11
12 1060 arrowhead is positioned midway between the centroid of the bar crests as imaged on
13
14
15 1061 8 and 12 June 2017.

16
17
18 1062 Figure 17: Distribution of unit sediment transport rates for both dunes ($n = 255$, using
19
20 1063 repeat UAV imagery from June 2017 in patches of SS3 reach) and bars ($n = 295$,
21
22 1064 repeat MAV sorties for the whole 18 km-long reach in June 2017).

23
24
25 1065 Figure 18: (A-C) Example Planet.com images of the South Saskatchewan River
26
27 1066 acquired in the same period as the specially-commissioned aerial (MAV) flight
28
29 1067 sorties together with tracing of unit bar crests; (D) calculated bar migration rates (see
30
31 1068 text for methodology) for unit bars using the Planet.com satellite imagery compared
32
33 1069 to measurements from MAV aerial imagery. (E) Inset shows bar migration rates
34
35 1070 derived from the Planet.com images for two different temporal gaps between
36
37 1071 images, illustrating the shorter (5-day) interval is unable to resolve migration rates
38
39 1072 less than $\sim 0.06 \text{ m hr}^{-1}$. Determination of migration rates must thus be considered
40
41
42 1073 with respect to pixel resolution and temporal frequency of images.
43
44
45
46
47 1074

1075

1076 **Table Captions**

1077 Table 1: Image properties for aerial (MAV) sorties over the South Saskatchewan

1078 River, near Outlook, Canada

1079 Table 2: eBee RTK and eBee Plus epochs collected during the 2016 and 2017 field

1080 seasons

1081 Table 3: Depth-brightness model properties for each reach

1082 Table 4: Error statistics for DSMs produced from MAV imagery; mean error (ME),

1083 root mean square error (RMSE) standard deviation of error (SDE) and the minimum

1084 level of detection (LoD)

1085 Table 5: Compilation of error statistics from other studies, note that the different

1086 scales of the imagery (GSD) relate to the magnitudes of error. The DSMs in this

1087 paper are from imagery with a 0.06 m GSD. Error statistics are reported in metres

1088 Table 6: Dune migration rate measured in different sized patches for sequential UAV

1089 images in 2015, 2016 and 2017. See Figure 3 for reach and patch locations



Figure 1: A) location within Canada, B) study site location within Saskatchewan Province, C) upstream and downstream reaches at study site including the three study reaches described in this paper: SS1, SS2 and SS3, and D) close up of upstream and downstream reaches (taken in 2016).

89x222mm (300 x 300 DPI)

1
2
3
4
5
6
7
8
9
10
11
12
13
14
15
16
17
18
19
20
21
22
23
24
25
26
27
28
29
30
31
32
33
34
35
36
37
38
39
40
41
42
43
44
45
46
47
48
49
50
51
52
53
54
55
56
57
58
59
60

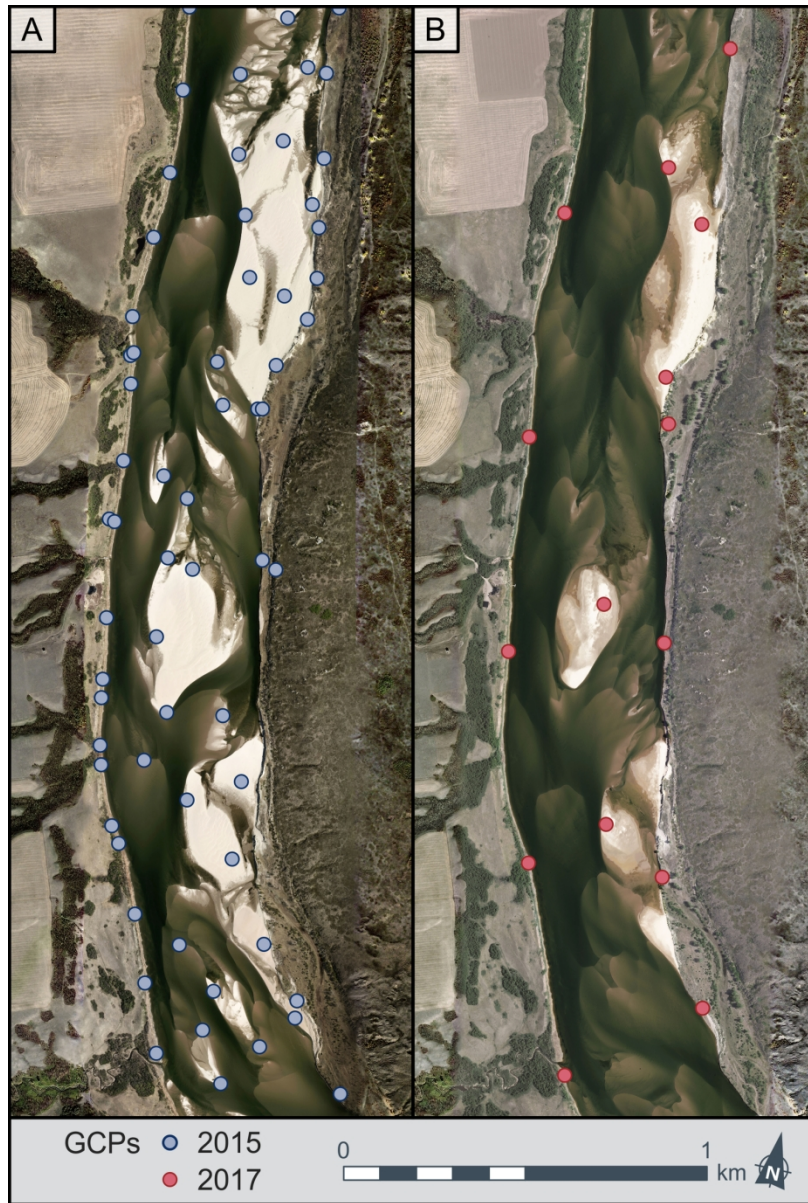


Figure 2: Distribution of GCPs on 2015 upstream and 2017 upstream reaches.

132x196mm (300 x 300 DPI)



Figure 3: A) location of 2016 dune migration measurements in SS1 and SS2 reaches and B) 2017 dune migration measurements in SS3 reach. Dotted line shows the boundary of UAV coverage.

156x163mm (300 x 300 DPI)

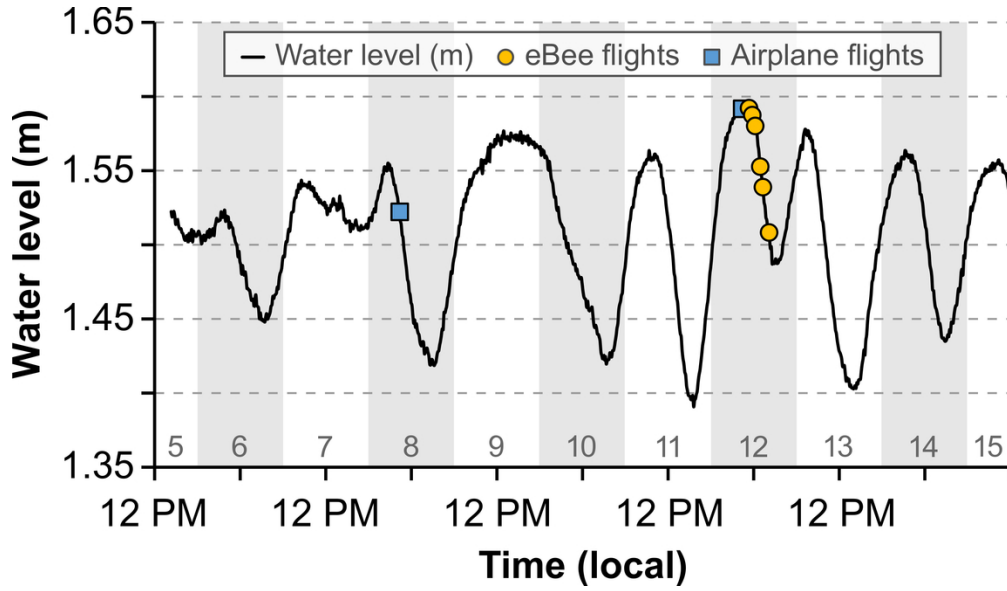


Figure 4: Water level variations during the 2017 field season and at the times of airplane and UAV flights. Notice the daily variations in water level associated with the release of water from the Gardiner Dam.

48x28mm (600 x 600 DPI)

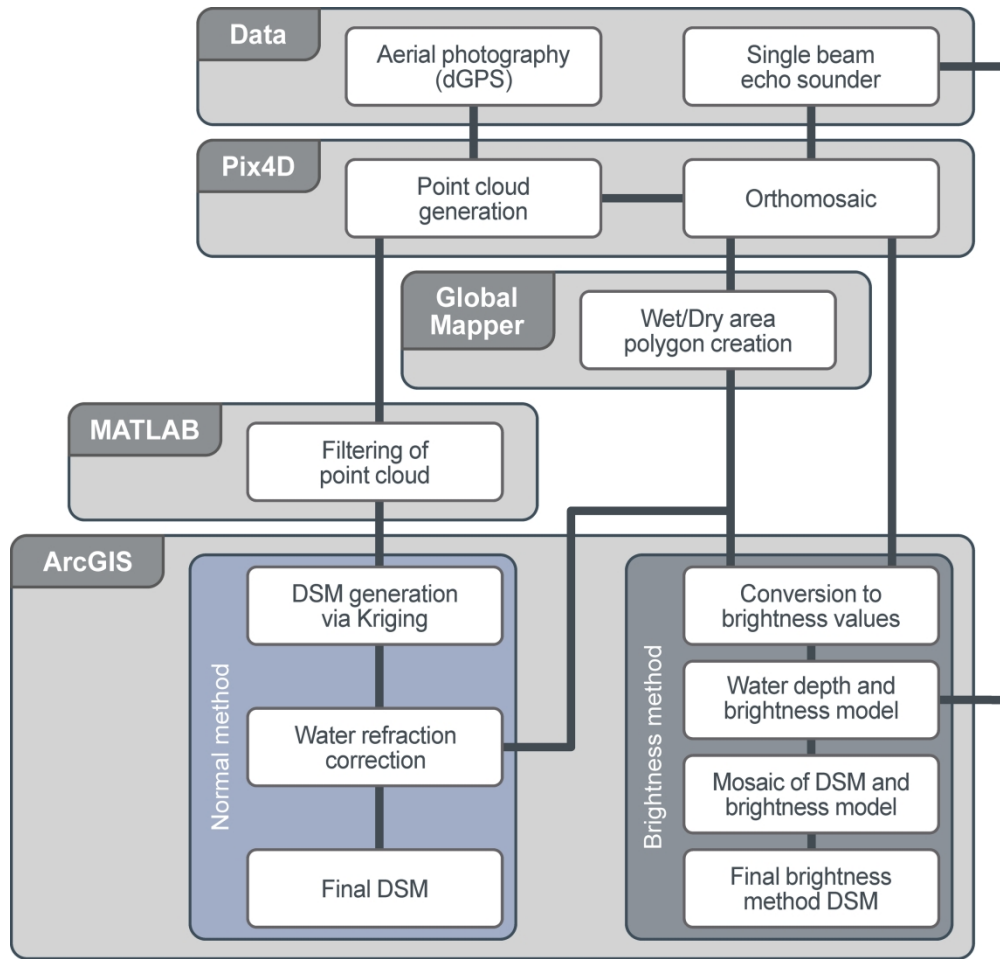


Figure 5: Workflow of DSM production from aerial images and the various data sources and computer programmes employed.

122x117mm (600 x 600 DPI)

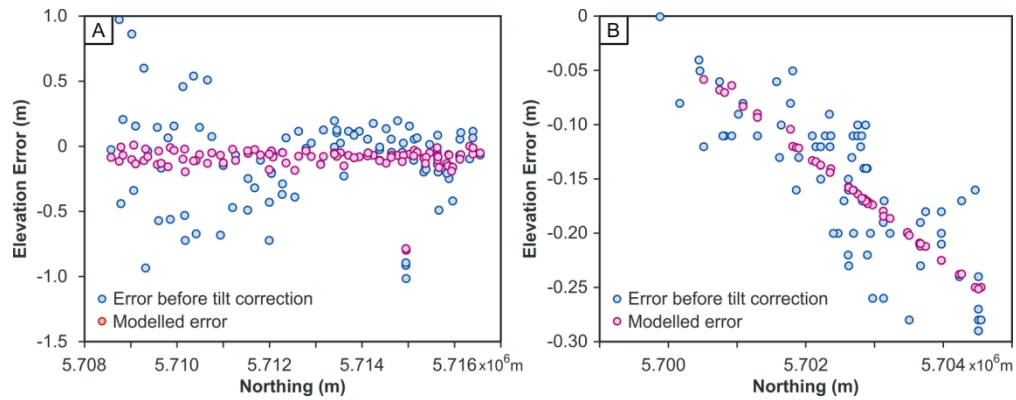


Figure 6: Elevation error plotted against Northing value for DSMs that are free from systematic tilt error (A) and which contain systematic tilt error (B). Blue circles represent the elevation error (difference between DSM and GCP elevation values) prior to tilt correction. Red circles represent the modelled error plane that is used to correct the DSM for the presence of systematic tilt

69x26mm (600 x 600 DPI)

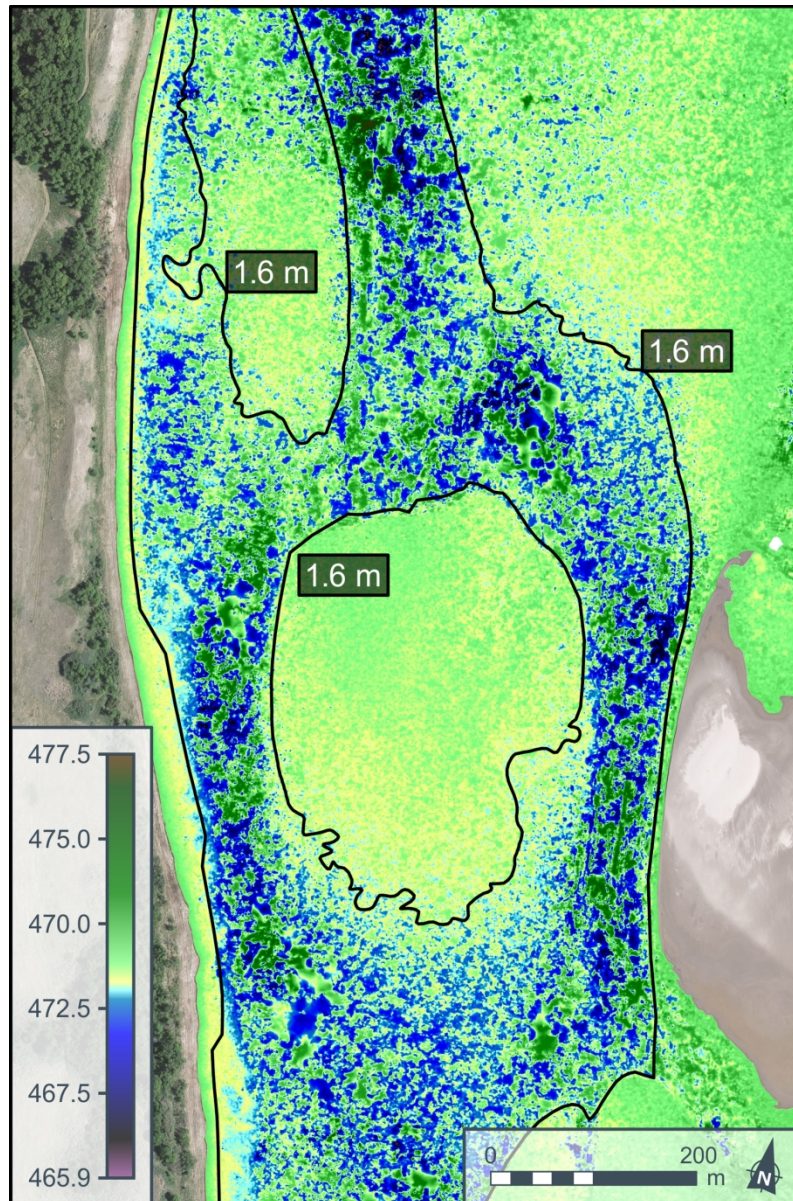


Figure 7: SfM becomes unreliable in producing bed elevations when water depths are greater than 1.6 m, thus justifying the need for a depth-brightness model. Note the scale is the local (z) datum and the boundary of 1.6 m depth has been superimposed to show the inconsistency of submerged bed elevations when only SfM is employed.

134x202mm (300 x 300 DPI)

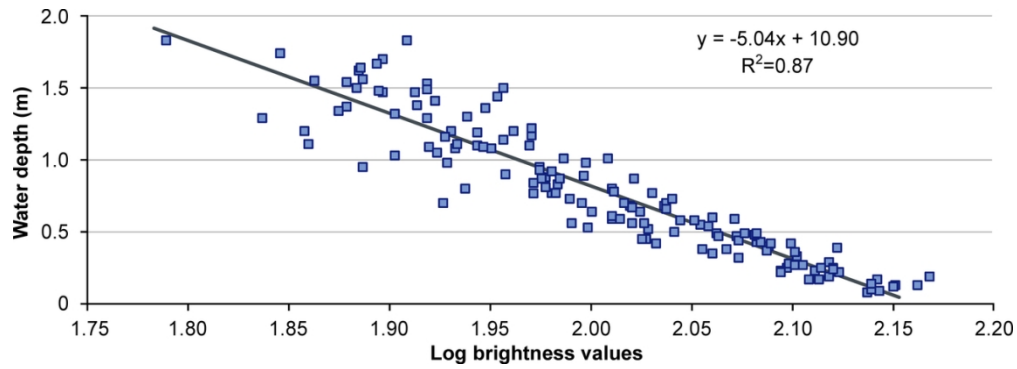


Figure 8: An example of a depth-brightness model used to create river bed depths from aerial (MAV) orthomosaics. This particular model is for the June 8th 2017 flight and was created using SBES depth measured points.

56x19mm (600 x 600 DPI)

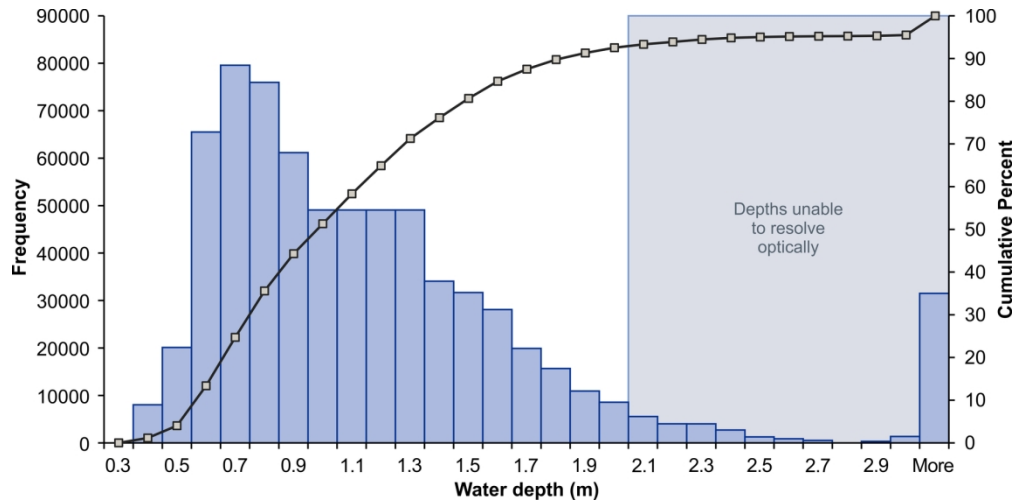


Figure 9: Histogram of SBES depths collected during the 2016 field season, note that very few depths (7.5%) are greater than 2 m.

81x40mm (600 x 600 DPI)

1
2
3
4
5
6
7
8
9
10
11
12
13
14
15
16
17
18
19
20
21
22
23
24
25
26
27
28
29
30
31
32
33
34
35
36
37
38
39
40
41
42
43
44
45
46
47
48
49
50
51
52
53
54
55
56
57
58
59
60

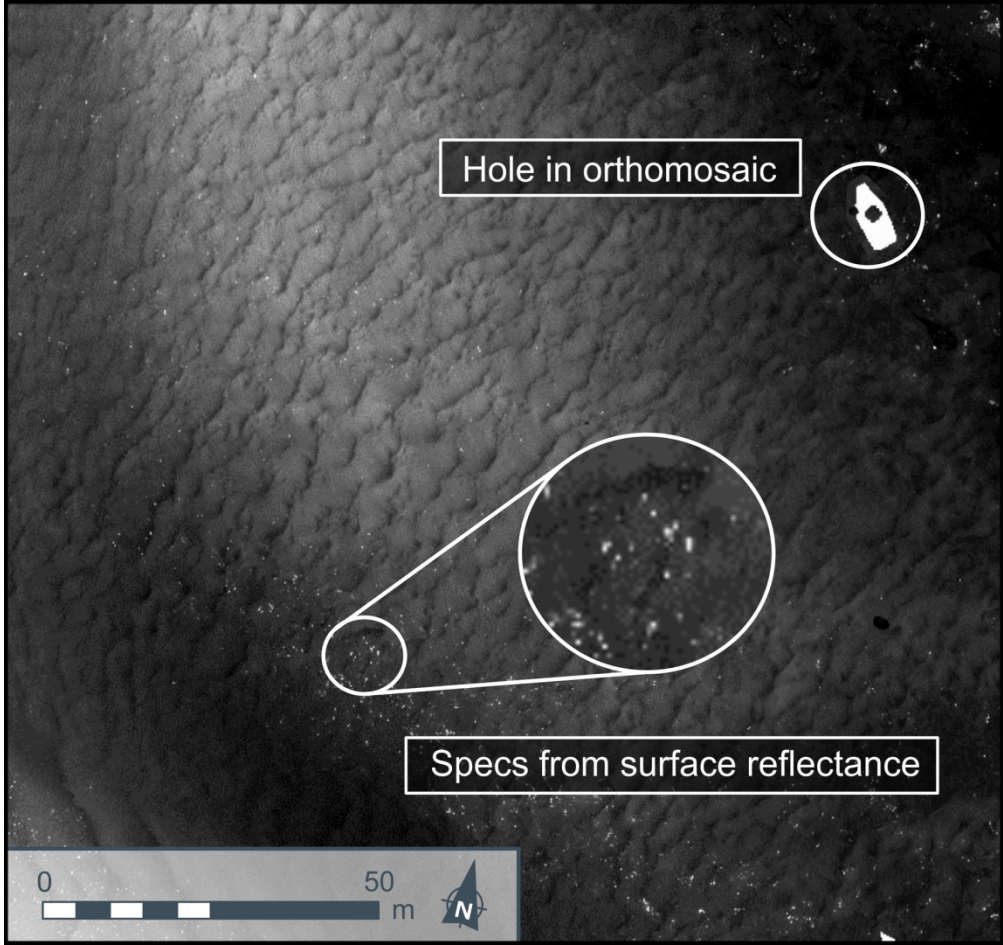


Figure 10: Issue with the depth-brightness model showing specks from surface shimmer and holes from the orthomosaic.

84x79mm (600 x 600 DPI)

1
2
3
4
5
6
7
8
9
10
11
12
13
14
15
16
17
18
19
20
21
22
23
24
25
26
27
28
29
30
31
32
33
34
35
36
37
38
39
40
41
42
43
44
45
46
47
48
49
50
51
52
53
54
55
56
57
58
59
60

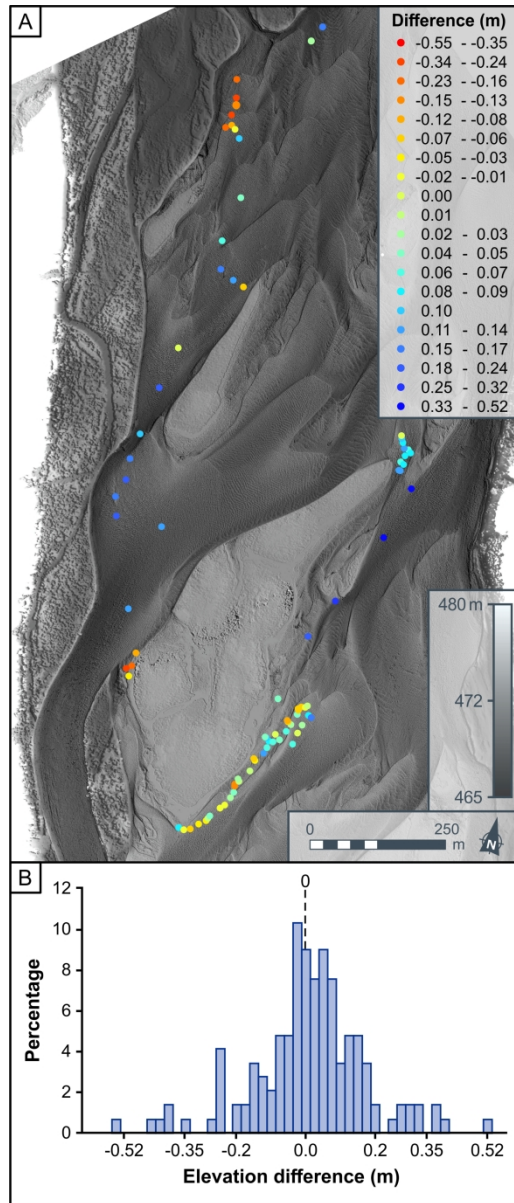


Figure 11: A) Example of points from depth measured error, and B) histogram for the June 8th DSM 2017.

198x460mm (300 x 300 DPI)

1
2
3
4
5
6
7
8
9
10
11
12
13
14
15
16
17
18
19
20
21
22
23
24
25
26
27
28
29
30
31
32
33
34
35
36
37
38
39
40
41
42
43
44
45
46
47
48
49
50
51
52
53
54
55
56
57
58
59
60

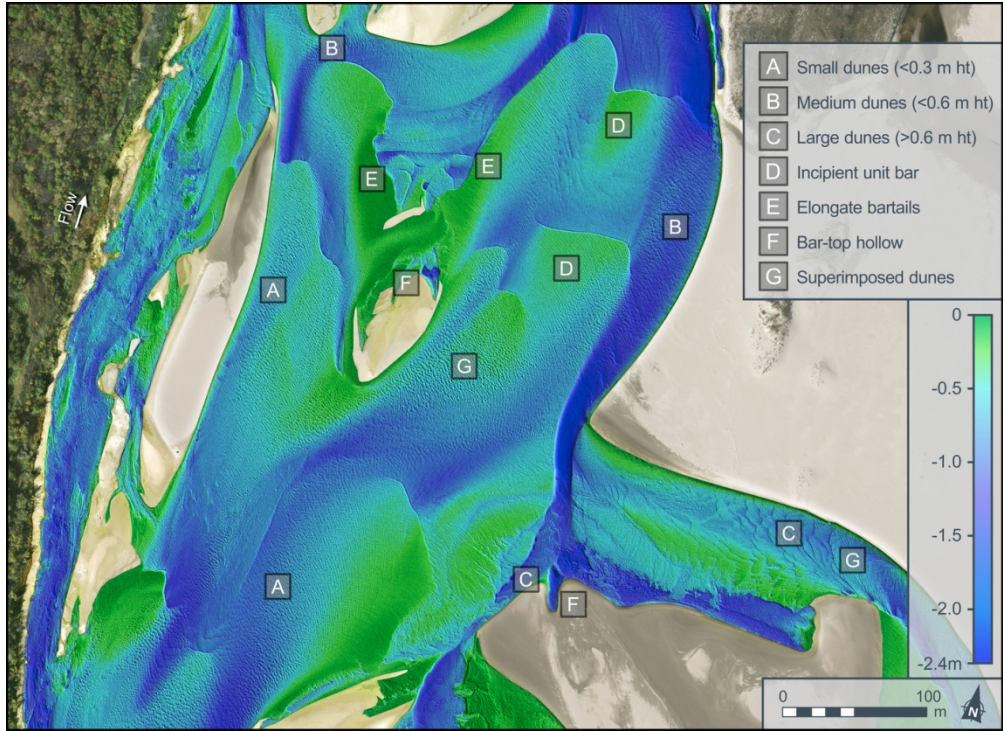
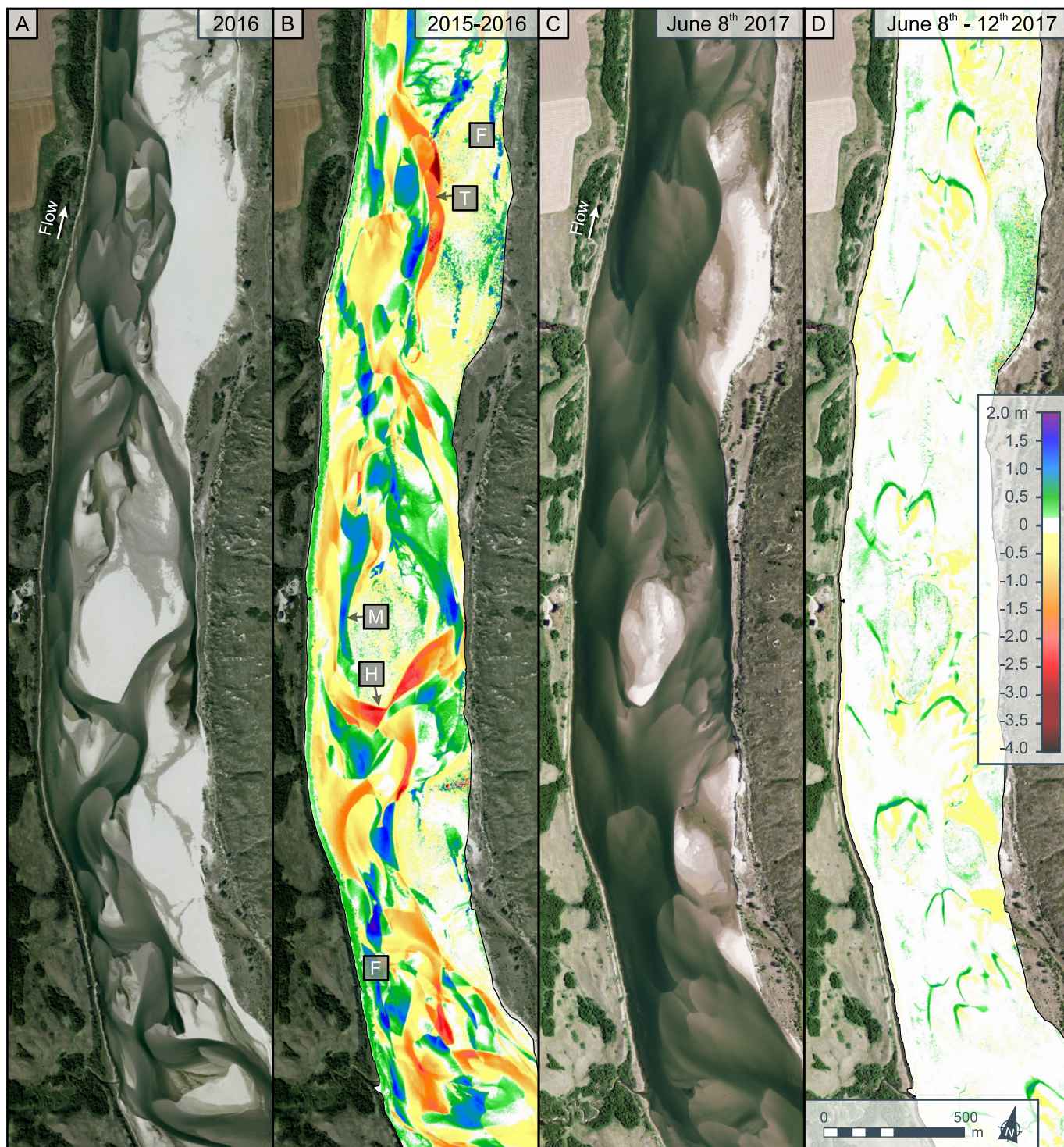


Figure 12: River bed depths superimposed on the orthomosaic showing detail of the various sand bedforms (see key). Location of image is in reach SS1 (see Figure 3A)

119x86mm (300 x 300 DPI)



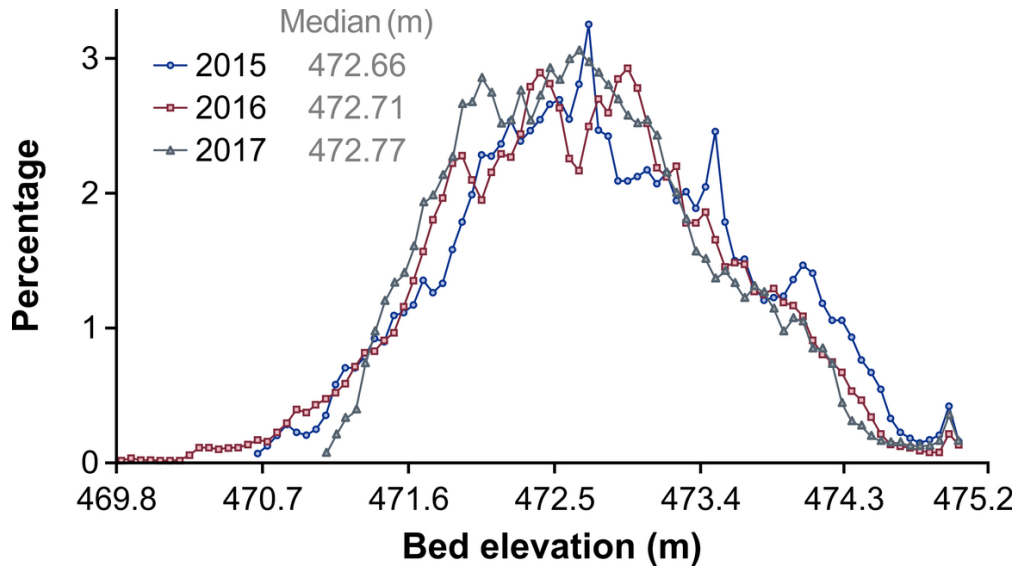


Figure 14: Elevation distributions for the 2015, 2016, and 2017 upstream reaches.

49x27mm (600 x 600 DPI)

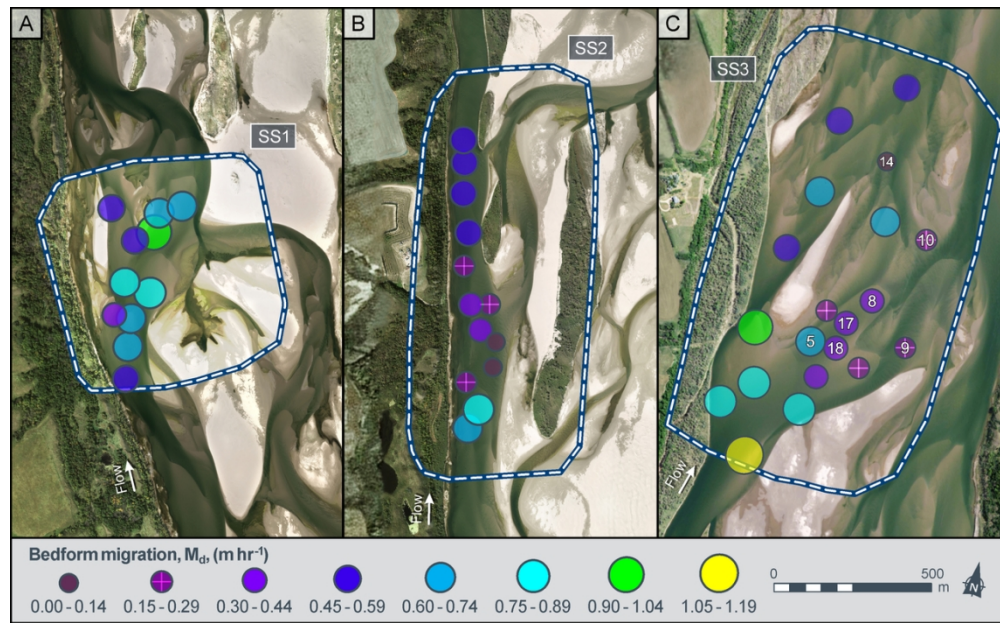


Figure 15: Dune migration rates for reaches SS1 (A), SS2 (B) and SS3 (C). Labels within circles in Figure 15C refer to the measurement patches also described in Table 6.

110x68mm (300 x 300 DPI)

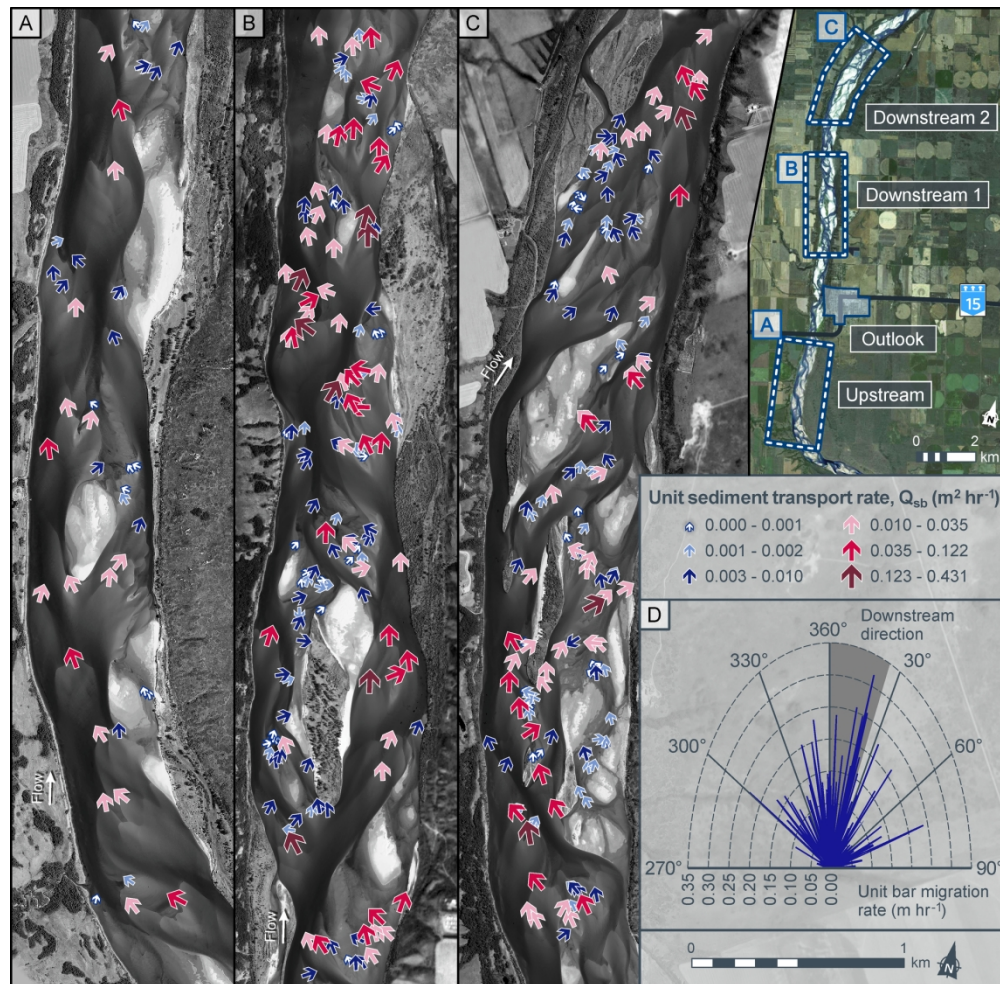


Figure 16: Bar unit sediment transport rates calculated from repeat airplane sorties in June 2017 for the upstream reach (A), the first half of the downstream reach (B), and the last half of the downstream reach (C). Unit bar migration rates and directions for all the bars shown in Figures 16A-C are shown in (D). Note the centre of the arrowhead is positioned midway between the centroid of the bar crests as imaged on 8 and 12 June 2017.

169x165mm (300 x 300 DPI)

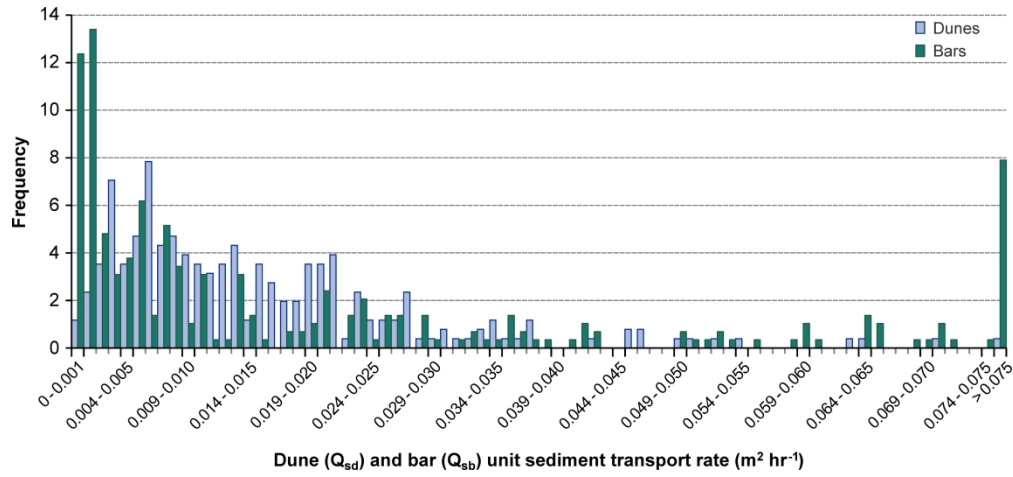


Figure 17: Distribution of unit sediment transport rates for both dunes ($n = 255$, using repeat UAV imagery from June 2017 in patches of SS3 reach) and bars ($n = 295$, repeat MAV sorties for the whole 18 km-long reach in June 2017).

173x80mm (600 x 600 DPI)

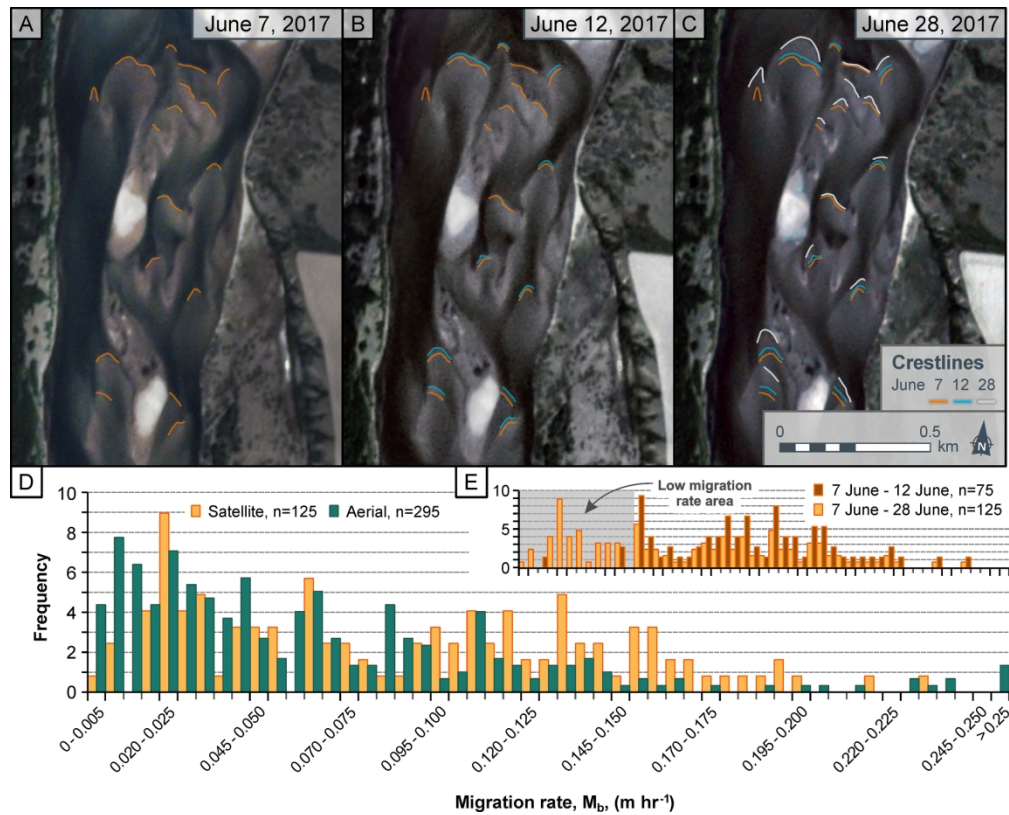


Figure 18: (A-C) Example Planet.com images of the South Saskatchewan River acquired in the same period as the specially-commissioned aerial (MAV) flight sorties together with tracing of unit bar crests; (D) calculated bar migration rates (see text for methodology) for unit bars using the Planet.com satellite imagery compared to measurements from MAV aerial imagery. (E) Inset shows bar migration rates derived from the Planet.com images for two different temporal gaps between images, illustrating the shorter (5-day) interval is unable to resolve migration rates less than $0.06\ m\ hr^{-1}$. Determination of migration rates must thus be considered with respect to pixel resolution and temporal frequency of images.

178x143mm (300 x 300 DPI)

| Date | Focal length (mm) | Aerial platform altitude (m) | Number of images ¹ | Number of GCPs | GSD (cm) | Image overlap |
|--------------|-------------------|------------------------------|-------------------------------|----------------|----------|---------------|
| 13 May 2015 | 100.50 | 1524 | 74 | 76 | 6 | 2-3 |
| 2 Sept. 2016 | 100.50 | 1524 | 142 | 227 | 6 | 2-3 to 4-5 |
| 8 June 2017 | 100.50 | 1493 | 160 | 58 | 6 | 2-3 to 4-5 |
| 12 June 2017 | 100.50 | 1493 | 160 | 58 | 6 | 2-3 to 4-5 |

¹Extra flight line added to 2016 and 2017 missions greatly increased the number of images.
2017 missions extended downstream accounting for the increased number as compared to 2016

| Date | Flight | Flight start (CST) | Flight finish (CST) | Flight Time (min) | Total Images | Matched Images | Match Percentage | GSD (cm) | Area (km ²) |
|----------------------------|--------|--------------------|---------------------|-------------------|--------------|----------------|------------------|----------|-------------------------|
| SS1 8 Sept. 2016 | 1 | 2:20 PM | 2:38 PM | 18 | 209 | 206 | 98.6 | 2.99 | 0.34 |
| | 2 | 2:53 PM | 3:10 PM | 17 | 206 | 200 | 97.1 | 2.99 | 0.33 |
| | 3 | 3:52 PM | 4:10 PM | 18 | 208 | 202 | 99.1 | 2.99 | 0.36 |
| SS2 9 Sept. 2016 | 1 | 11:08 AM | 11:25 PM | 17 | 189 | 188 | 99.5 | 2.50 | 0.42 |
| | 2 | 11:37 AM | 12:04 PM | 27 | 332 | 319 | 96.1 | 2.57 | 0.44 |
| | 3 | 12:44 PM | 1:10 PM | 26 | 347 | 344 | 99.1 | 2.60 | 0.47 |
| SS3 12 June 2017 | 1 | 9:38 AM | 10:22 AM | 44 | 859 | 820 | 95.5 | 2.69 | 0.77 |
| | 2 | 10:33 AM | 11:16 AM | 43 | 874 | 734 | 84.0 | 2.71 | 0.77 |
| | 3 | 11:24 AM | 12:06 AM | 42 | 821 | 704 | 85.7 | 2.66 | 0.73 |
| | 4 | 12:47 PM | 1:29 PM | 42 | 838 | 803 | 95.8 | 2.65 | 0.77 |
| | 5 | 1:32 PM | 2:14 PM | 42 | 834 | 793 | 95.1 | 2.66 | 0.80 |

1
2
3
4
5
6
7
8
9
10
11
12
13
14
15
16
17
18
19
20
21
22
23
24
25
26
27
28
29
30
31
32
33
34
35
36
37
38
39
40
41
42
43
44
45
46
47
48
49
50
51
52
53
54
55
56
57
58
59
60

| Date and reach | Depth brightness-model | R ² | p value | n |
|---------------------|---------------------------|----------------|---------|-------|
| 13 May 2015 | $y = -5.50x + 10.64$ | 0.81 | 0.000 | 717 |
| 2 Sept. 2016 - Up | $y = -4.65x + 09.38$ | 0.82 | 0.000 | 56888 |
| 2 Sept. 2016 - Down | $y = -4.72x + 09.34$ | 0.77 | 0.000 | 56386 |
| 8 June 2017 | $y = -5.04x + 10.90$ | 0.87 | 0.000 | 144 |
| 12 June 2017 | $y = -5.03x + 10.99$ | 0.81 | 0.000 | 144 |

| Date and reach | DSM metrics | | | | | DSMs of difference | |
|---------------------------|-------------|--------|----------|---------|---------|----------------------------|---------|
| | n | ME (m) | RMSE (m) | SDE (m) | SDE/GSD | Dates | LoD (m) |
| 13 May 2015 - Upstream | 76 | -0.02 | 0.08 | 0.08 | 1.33 | 2016 Sept. 2 - 2015 May 13 | 0.13 |
| 2 Sept. 2016 - Upstream | 58 | 0.02 | 0.10 | 0.10 | 1.67 | 2017 June 8 - 2016 Sept. 2 | 0.12 |
| 8 June 2017 - Upstream | 17 | -0.03 | 0.07 | 0.07 | 1.67 | 2017 June 12 - 8 | 0.13 |
| 12 June 2017 - Upstream | 17 | -0.10 | 0.15 | 0.11 | 1.83 | | |
| 13 May 2015 - Downstream | 13 | -0.22 | 0.29 | 0.19 | 3.17 | 2016 Sept. 2 - 2015 May 13 | 0.27 |
| 2 Sept. 2016 - Downstream | 61 | -0.02 | 0.19 | 0.19 | 3.17 | 2017 June 8 - 2016 Sept. 2 | 0.22 |
| 8 June 2017 - Downstream | 40 | 0.00 | 0.12 | 0.12 | 2.00 | 2017 June 12 - 8 | 0.16 |
| 12 June 2017 - Downstream | 40 | -0.07 | 0.13 | 0.12 | 2.00 | | |

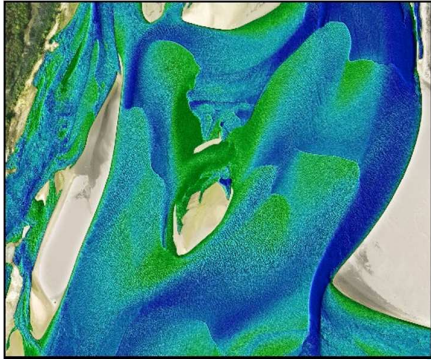
| Previous publications | GSD (m) | RMSE (m) | ME (m) | M _d (m) | SDE/ GSD |
|--|-------------|-------------|-----------|-----------------------|-------------|
| Lane <i>et al.</i> (2010) | 0.19 | N/A | -0.23 | 0.28 | 1.47 |
| Javernick <i>et al.</i> (2014) | 0.12 | 0.13 | 0.03 | 0.13 | 1.08 |
| Smith <i>et al.</i> (2014) | N/A | 0.03 | 0 | 0.06 | N/A |
| Dietrich (2016) | 0.05 - 0.07 | 0.73 | -0.08 | 0.11 | 1.83 |
| Bakker & Lane (2017) ¹ | 0.35 | 0.38 | 0.02 | 0.74 | 2.11 |
| Carbonneau & Dietrich (2017) ² | 0.03/0.03 | N/A | 0.05/0.01 | 0.24/0.03 | 8/1 |
| Cook (2017) | 0.02 - 0.03 | 0.30 | 0.12 | 0.15 | 5.00 |
| James <i>et al.</i> (2017) ³ | 0.19 | 0.24 | 0.09 | N/A | N/A |
| Westaway <i>et al.</i> (2010) | 0.04 | N/A | -0.03 | 0.12 | 3.00 |
| Present study (12 June 2017 - downstream) | 0.04 | N/A | -0.03 | 0.12 | 2.00 |

¹2005 DEM, ²2017 Site A/B, ³2013 DEM

1
2
3
4
5
6
7
8
9
10
11
12
13
14
15
16
17
18
19
20
21
22
23
24
25
26
27
28
29
30
31
32
33
34
35
36
37
38
39
40
41
42
43
44
45
46
47
48
49
50
51
52
53
54
55
56
57
58
59
60

| Reach | Patch Number | Patch Size (m ²) | Number of Dunes | Mean Patch Migration Rate (m hr ⁻¹) | St. dev. (m hr ⁻¹) |
|---------------------|--------------|------------------------------|-----------------|---|--------------------------------|
| SS1 2016 | 1 | 360 | 15 | 0.54 | 0.10 |
| | 2 | 620 | 50 | 0.62 | 0.13 |
| | 3 | 365 | 50 | 0.69 | 0.13 |
| | 4 | 360 | 40 | 0.44 | 0.07 |
| | 5 | 365 | 22 | 0.88 | 0.11 |
| | 6 | 365 | 38 | 0.77 | 0.10 |
| | 7 | 365 | 42 | 0.56 | 0.05 |
| | 8 | 365 | 15 | 0.93 | 0.13 |
| | 9 | 365 | 40 | 0.73 | 0.15 |
| | 10 | 365 | 41 | 0.72 | 0.14 |
| | 11 | 365 | 30 | 0.59 | 0.10 |
| SS2 2016 | 1 | 900 | 25 | 0.67 | 0.18 |
| | 2 | 900 | 64 | 0.79 | 0.18 |
| | 3 | 3000 | 35 | 0.24 | 0.12 |
| | 4 | 900 | 19 | 0.06 | 0.02 |
| | 4A | 900 | 7 | 0.10 | 0.03 |
| | 5 | 900 | 35 | 0.32 | 0.10 |
| | 6 | 1500 | 36 | 0.22 | 0.09 |
| | 7 | 1800 | 50 | 0.35 | 0.09 |
| | 8 | 900 | 16 | 0.20 | 0.07 |
| | 8A | 1800 | 35 | 0.47 | 0.15 |
| | 9 | 900 | 36 | 0.47 | 0.13 |
| SS3 2017 | 10 | 1500 | 89 | 0.43 | 0.13 |
| | 11 | 900 | 49 | 0.53 | 0.15 |
| | 1 | 760 | 9 | 1.15 | 0.33 |
| | 2 | 1223 | 13 | 0.79 | 0.20 |
| | 3 | 1582 | 20 | 0.83 | 0.15 |
| | 4 | 1591 | 12 | 0.75 | 0.14 |
| | 5 | 1593 | 11 | 0.62 | 0.08 |
| | 6 | 906 | 15 | 0.91 | 0.09 |
| | 7 | 1849 | 14 | 0.20 | 0.03 |
| | 8 | 1827 | 12 | 0.33 | 0.11 |
| | 9 | 5128 | 11 | 0.20 | 0.06 |
| 10 | 1959 | 12 | 0.26 | 0.25 | |
| 11 | 341 | 14 | 0.66 | 0.17 | |
| 12 | 713 | 15 | 0.51 | 0.06 | |
| 13 | 1376 | 13 | 0.61 | 0.06 | |
| 14 | 2897 | 12 | 0.13 | 0.06 | |
| 15 | 1370 | 14 | 0.46 | 0.12 | |
| 16 | 1781 | 9 | 0.52 | 0.08 | |
| 17 | 2234 | 13 | 0.32 | 0.07 | |
| 18 | 1021 | 12 | 0.38 | 0.09 | |
| 19 | 3043 | 15 | 0.33 | 0.06 | |
| 20 | 1445 | 10 | 0.29 | 0.06 | |

1 Unit bar and dune dynamics are quantified for the sandy braided South Saskatchewan
2 River, Canada, using images captured from aeroplane, unmanned aerial vehicle (UAV)
3 and satellite platforms. Dune and unit bar migration rates are spatially variable in response
4 to local planform morphology. Sediment transport rates can be estimated for dunes and
5 unit bars using plane and UAV images and Digital Surface Models (DSMs) but just 2D
6 imagery, including from satellite platforms, may provide reasonable first-order estimates of
7 bed sediment flux.
8
9



23
24
25 **Quantification of bedform dynamics and bedload sediment flux in sandy braided**
26 **ivers from airborne and satellite imagery**

27
28 Robert Strick, Philip Ashworth*, Gregory Sambrook Smith, Andrew Nicholas, James Best,
29 Stuart Lane, Daniel Parsons, Christopher Simpson, Christopher Unsworth and Jonathan
30 Dale
31

32
33 *corresponding author
34
35
36
37
38
39
40
41
42
43
44
45
46
47
48
49
50
51
52
53
54
55
56
57
58
59
60